Commun Nonlinear Sci Numer Simulat 91 (2020) 105394

Contents lists available at ScienceDirect

Commun Nonlinear Sci Numer Simulat

journal homepage: www.elsevier.com/locate/cnsns

Research paper

Nonlinear energy harvester with coupled Duffing oscillators

Danilo Karličić[a,b], Milan Cajić[b], Stepa Paunović[b], Sondipon Adhikari[a,*]

[a] College of Engineering, Swansea University, United Kingdom
[b] Mathematical institute of the Serbian Academy of Sciences and Arts, Kneza Mihaila 36, Belgrade, Serbia

ARTICLE INFO

Article history:
Received 15 February 2020
Revised 11 May 2020
Accepted 4 June 2020
Available online 11 June 2020

Keywords:
Nonlinear vibrations
Energy harvesting
Base amplitude
Force responses
Nonlinear energy sink
Energy localization
Incremental harmonic balance method
Continuation technique

ABSTRACT

Structural vibrations are very common in aerospace and mechanical engineering systems, where dynamic analysis of modern aerospace structures and industrial machines has become an indispensable step in their design. Suppression of unwanted vibrations and their exploitation for energy harvesting at the same time would be the most desirable scenario. The dynamical system presented in this communication is based on a discrete model of energy harvesting device realized in such a manner as to achieve both vibration suppression and harvesting of vibration energy by introducing the nonlinear energy sink concept. The mechanical model is formed as a two-degree of freedom nonlinear oscillator with an oscillating magnet and harmonic base excitation. The corresponding mathematical model is based on the system of nonlinear nonhomogeneous Duffing type differential equations. To explore complex dynamical behaviour of the presented model, periodic solutions and their bifurcations are found by using the incremental harmonic balance (IHB) and continuation methods. For the detection of unstable periodic orbits, the Floquet theory is applied and an interesting harmonic response of the presented nonlinear dynamical model is detected. The main advantage of the presented approach is its ability to obtain approximated periodic responses in terms of Fourier series and estimate the voltage output of an energy harvester for a system with strong nonlinearity. The accuracy of the presented methodology is verified by comparing the results obtained in this work with those obtained by a standard numerical integration method and results from the literature. Numerical examples show the effects of different physical parameters on amplitude-frequency, response amplitude - base amplitude and time response curves, where a qualitative change is explored and studied in detail. Presented theoretical results demonstrate that the proposed system has advanced performance in both system requirements - vibration suppression, and energy harvesting.

1. Introduction

In vibration theory, the concept of dynamic absorbers has a long history and it was initiated in [1] as a device based on additional mass and spring attached to the main structure. The main property of such devices is the transfer of vibration energy from the main structure to the tuned vibration absorber. It was demonstrated that nonlinear vibration absorbers are more effective in vibration absorption than the linear ones since they can cover a wider frequency range. The term nonlinear energy sink (NES) was introduced in [2] for a single degree of freedom lumped-mass system with strong nonlinear

* Corresponding author.
E-mail address: s.adhikari@swansea.ac.uk (S. Adhikari).

https://doi.org/10.1016/j.cnsns.2020.105394
1007-5704/

stiffness and weak linear damping attached to the primary structure with liner or nonlinear properties. Due to their exceptional properties and robust design, nonlinear energy sinks have been widely used in engineering practice over the last two decades with applications ranging from vibration control and suppression to energy harvesting purposes.

Subsequently, in [3] the authors proposed many different configurations of nonlinear absorbers based on the continuous (rod, beam, plate) and discrete structures (lumped mass models) with nonlinear single and multiple degrees of freedom attachments. By using analytical, numerical, and experimental methods, they have studied the targeted energy transfer for different models of a nonlinear energy sink in coupled discrete and continuous structural vibration systems. The key concept of a nonlinear energy sink device is to transfer energy from a primary structure to the nonlinear attachment i.e. nonlinear energy sink, for the entire frequency band, especially in the resonance regime where the energy and vibration amplitudes are at the highest level [4]. This phenomenon is also known as energy pumping. Moreover, in [4] the authors proposed a wide spectrum of applications of this physical phenomenon as a concept for passive energy transfer in complex fluid flow, nonlinear acoustics, or simple mechanical models. On the other hand, the authors in [5] performed a systematic review of different approaches used in the design and analysis of nonlinear dissipative devices, known as "nonlinear dampers", that appear in structural vibration control practices. Based on the aforementioned, NES belongs to a subgroup of "nonlinear dampers", which is a more general term for nonlinear models used in vibration absorption of complex mechanical systems. The authors in [5] divided "nonlinear dampers" into three main groups, (i) Nonlinear Energy Sinks (NESs), (ii) Particle Impact Dampers (PIDs), and Nonlinear Viscous Dampers (NVDs), and provided a detailed explanation on how damping phenomenon occurs in all three subgroups. In the following, the focus will be kept on the NES model and its application in vibration suppression and energy harvesting (EH).

Genedelman and colleagues [6–8] proposed systematic analytical and numerical approaches for the analysis of a harmonically excited NES system. By introducing the nonlinear normal mode concept, Genedelman [6] investigated the energy distribution in a highly asymmetric two-degree of freedom system, which consists of coupled linear and highly nonlinear damped oscillators employed as NES. Special attention is devoted to the mechanisms of subharmonic resonance and energy transfer to the nonlinear normal modes. Subsequently, in [7,8] the authors performed bifurcation analyses of NES models by using the combination of the invariant manifold approach and multiple scales methods, as well as the averaging method. On the other hand, the numerical continuation technique in combination with the harmonic balance and shooting method was introduced in [9] to investigate the bifurcation and stability of periodic orbits of NES with weak nonlinearity and linear damping. They traced frequency - amplitude response curves and detected different bifurcation points such as fold, Hopf, symmetry braking, and period of doubling bifurcation, which leads to the conclusion that energy transfer is bounded i.e. it is not possible when damping and nonlinearity in weakly coupled systems have small values. In [10], the authors suggested the NES model for passive flutter control of a rigid wing with structural nonlinearity, which belongs to a special class of NESs used in aeroelasticity problems. They focused their investigation on the multi-degree of freedom NES by explaining the details of an energy transfer to NES through the phenomenon of nonlinear modal interaction. In another study [11], a normal form analytical approach is used to analyse the flutter control and suppression of limit cycle oscillations in an aeroelastic system with NES. Furthermore, in [12] the authors performed advanced numerical simulations to determine the NES limits and provide the effective control of transonic flutter. Moreover, vortex-induced vibrations are one of the most interesting problems where the concept of NES was introduced to absorb vibration energy from a primary structure, as presented in [13,14].

It should be noted that there are two main categories of nonlinear energy harvesting devices, the first one belongs to mono-stable and the second one to bi-stable harvesters. The general difference between these two concepts is in the potential energy function of the system, where the mono-stable system has a single stable equilibrium while the bi-stable system has two stable equilibrium points separated by a potential barrier. An outstanding monograph [15] was published as a comprehensive study of energy harvesting problems based on the piezoelectric effect. They investigated a wide spectrum of EH models ranging from linear, to stochastic and nonlinear regimes of vibration, which represents a remarkable source of fundamental research and application of EH systems. Because of the unique mechanical concept, NES models can be very useful in EH [16–18], where it is possible to have simultaneous vibration suppression and energy harvesting. There are two main directions in the application of NES in combination with EH. The first one includes NES with piezoelectric effects [19] while the second one is based on the electromagnetic effect [20]. In [21], the authors suggested a novel piezoelectric EH device based on the NES concept to achieve simultaneous broadband energy harvesting from a nonlinear energy sink and vibration suppression of the primary structure. By using the numerical method and nonlinear normal form, they investigated the transient behaviour and energy transfer at 1: 1 resonance and demonstrated effective performance of NES with quasi-essentially nonlinear stiffness. By introducing the mixed multi-scale and harmonic balance methods as well as the Newton - Raphson harmonic balance method, nonlinear dynamic behaviour of a piezoelectric vibration energy harvester working in conjunction with the NES mechanism was investigated in [22]. The authors demonstrated remarkable properties of the proposed nonlinear energy sink - energy harvesting (NES-EH) model, where the energy localized branch in the multi-valued region looks very promising in terms of the energy absorbed from a primary structure and the improvement of energy conversion efficiency. Recently, some authors investigated a special class of NES-EH model based on the oscillating magnet between fixed coils, where both functions of such a device, vibration suppression and energy harvesting, are fulfilled [23,24]. For the investigation of complex dynamic behaviour, the MATCONT software is often used to obtain frequency responses of EH models or to validate numerical results experimentally. Introducing the analytical approximation method such as the complexification-averaging method, the steady-state regime of a giant magnetostrictive harvester integrated with a nonlinear

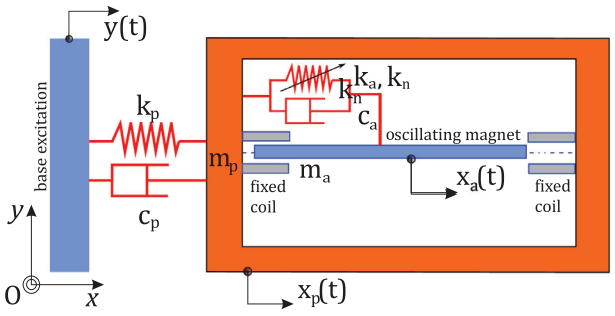

Fig. 1. The lumped-element model of a nonlinear energy sink - energy harvester device.

energy sink was investigated in [25] based on the previous study [20]. Moreover, by investigating the stability of periodic orbits, they detected the saddle-node bifurcation and derived the instability boundaries. On the other hand, the application of the Lyapunov function in the stability analysis with additional control can be used to extend the analysis of nonlinear discrete NES-EH systems, as given in [26,27].

The main objective of this paper is to provide a reliable methodology to analyse the complex dynamic behaviour of a strongly nonlinear NES-EH with varying the amplitude of external base excitation. The presented NES-EH model is based on a physically realized system given in [23] exhibiting both energy harvesting and vibration suppression through a nonlinear energy sink device. Herein, numerical simulations are carried out by the incremental harmonic balance (IHB) method in combination with the continuation technique to generate the response amplitude - base amplitude and frequency-amplitude response curves (i.e. bifurcation diagrams) that reveal a unique dynamic behaviour of the NES-EH system. Moreover, to detect stable and unstable periodic solution branches, the Floquet theory is introduced in combination with IHB. The main attention is pointed to the detection of amplitude response functions for different values of excitation frequency and system parameters, where multiple periodic solutions and unstable branches of periodic responses are detected. The application of the IHB method in combination with continuation technique for determination of the response amplitude - base amplitude is the key difference compared to the previous research [23]. The focus is directed to the determination of voltage responses of load resistors, which are shown to be significantly influenced by the excitation frequency, the nonlinear stiffness parameter, and the resistance load. Further analysis demonstrates how the system parameters affect the localization of the system's energy to the NES mass. The results obtained by the IHB method are verified against the Runge-Kutta method and also against the relevant results from the literature.

2. Nonlinear energy sink - energy harvester model

Let us consider the NES-EH device model formed as a two-mass system coupled by a nonlinear spring and a linear damper, which is subjected to external harmonic base excitation (see Fig. 1). In general, the device is based on two connected oscillators where m_p represents a primary mass of the main structure (linear oscillator) while m_a is the attached mass of the nonlinear absorber i.e. the nonlinear energy sink (nonlinear attachment). The terms k_p and c_p represent, respectively, the stiffness and the damping of the linear spring and dash-pot. The model proposed in this study is given as a two-degree of freedom NES, where masses m_p and m_a are connected through a nonlinear spring (with stiffness k_n) and a linear damper (with damping c_a). The total damping c_a consists of the mechanical c_{am} and electrical part c_e. The base is harmonically excited $y(t) = Y \sin \Omega t$, where Y is the amplitude and Ω is the excitation frequency. The energy harvesting mechanism for the conversion of the mechanical vibration to the electric energy and the corresponding voltage is based on the electromagnetic phenomenon, where the magnet axially oscillates between two coils placed on the main structure as shown in Fig. 1. Mathematical model of the simplified NES-EH model is given in the following form

$$m_p\ddot{x}_p + c_p\dot{x}_p + k_p x_p - c_a(\dot{x}_a - \dot{x}_p) - k_a(x_a - x_p) - k_n(x_a - x_p)^3 = k_p y(t) + c_p\dot{y}(t), \tag{1}$$

$$m_a\ddot{x}_a + c_a(\dot{x}_a - \dot{x}_p) + k_a(x_a - x_p) + k_n(x_a - x_p)^3 = 0, \tag{2}$$

where x_p and x_a are displacements of the linear subsystem and nonlinear attachment, while k_a and k_n are the linear and nonlinear stiffnesses, respectively. The time derivative $\dot{(\cdot)}$ is used to represent $d(\cdot)/dt$, while total damping c_a is given by the formula

$$c_a = c_e + c_{am} = \frac{k_t^2}{2R_{coil} + R_{load}} + c_{am}, \tag{3}$$

where k_t is the transduction factor, R_{coil} is the resistance of one coil and R_{load} is the resistance of the load resistor as given in [24]. As discussed in [24], estimated amount of harvested energy is equal to the summation of a power dissipated at the

load resistor over the time period T, which is given as

$$E_{load} = \int_0^T P_{load} dt, \tag{4}$$

where P_{load} is the power dissipated by the load resistor defined as

$$P_{load} = i(t)v(t) = i^2 R_{load} = \frac{k_t^2 R_{load}}{(2R_{coil} + R_{load})^2} \dot{z}^2, \tag{5}$$

where the term $z = (x_a - x_p)$ is the relative displacement between the displacements of the primary structure and NES attachment, $i(t)$ is the current induced in the coil and $v(t)$ is the corresponding voltage.

To analyse the periodic responses of the presented model and their bifurcations by using the IHB and continuation methods, we introduce some simplifications in Eq. (1). First, we introduce a new time scale $\tau = \Omega t$ and then a new coordinate $z = x_a - x_p$, which yields

$$\left(\frac{\Omega}{\omega_p}\right)^2 \ddot{x}_p + \Lambda\Omega\dot{x}_p + x_p - \lambda\Omega\dot{z} - kz - Kz^3 = Y\sin(\tau) + \Lambda\Omega Y\cos(\tau), \tag{6}$$

$$\left(\frac{\Omega}{\omega_a}\right)^2 (\ddot{x}_p + \ddot{z}) + \lambda\Omega\dot{z} + kz + Kz^3 = 0, \tag{7}$$

where new parameters are defined as

$$\omega_p = \sqrt{\frac{k_p}{m_p}}, \quad \omega_a = \sqrt{\frac{k_p}{m_a}}, \quad \Lambda = \frac{c_p}{k_p}, \quad \lambda = \frac{c_a}{k_p}, \quad k = \frac{k_a}{k_p}, \quad K = \frac{k_n}{k_p}.$$

and the time derivative operator $\dot{(\cdot)}$ takes on a new form $d(\cdot)/d\tau$.

3. The incremental harmonic balance method

The main advantages of the IHB method are the possibility for obtaining the semi-analytical solution of a system of nonlinear differential equations and an easy implementation of the continuation algorithm for tracing the responses curves. Moreover, in comparison to standard perturbation methods, there is no need to introduce a small scale parameter for systems with strong nonlinearity. In [28], the authors developed a methodology based on IHB method, Floquet theory and continuation method to analyse complex dynamic behaviour of a nonlinear dynamic system. Among others, an interesting application of this methodology to nonlinear problems in structural dynamics, especially to nonlinear vibration of beams [29–31], should be mentioned. However, the IHB method was applied in many other engineering problems ranging from the analysis of the nonlinear dynamic behaviour of a floating body [32] or the subharmonic resonance of a general piecewise-linear stiffness system [33], to the vibration suppression using a nonlinear energy sink [34]. In this paper, the main focus is pointed toward tracing the response amplitude - base amplitude and frequency-amplitude responses of the NES-EH model as well as the estimation of EH response voltage for different values of the amplitude of external base excitation and detection of bifurcation points. The first step in the IHB method is to introduce the incremental relations for Y, z and x_p,

$$Y = Y_0 + \Delta Y, \quad z(\tau) = z_0(\tau) + \Delta z(\tau), \quad x_p(\tau) = x_{p0}(\tau) + \Delta x_p(\tau), \tag{8}$$

where Y_0, z_0 and x_{p0} represent a known vibration state, and ΔY, Δz and Δx_p are the corresponding increments of the amplitude of excitation load and amplitudes of displacements z and x_p, respectively. By assuming the periodic solutions of the displacements $z(\tau)$ and $x_p(\tau)$, the functions $(z_0(\tau), \Delta z(\tau))$ and $(x_{p0}(\tau), \Delta x_p(\tau))$ can be taken in the Fourier series as

$$x_{p0}(\tau) = a_{10} + \sum_{n=1}^{N_h} [a_{1n}\cos(n\tau) + b_{1n}\sin(n\tau)] = \mathbf{C}\mathbf{A}_1, \tag{9}$$

$$\Delta x_p(\tau) = \Delta a_{10} + \sum_{n=1}^{N_h} [\Delta a_{1n}\cos(n\tau) + \Delta b_{1n}\sin(n\tau)] = \mathbf{C}\Delta\mathbf{A}_1,$$

$$z_0(\tau) = a_{20} + \sum_{n=1}^{N_h} [a_{2n}\cos(n\tau) + b_{2n}\sin(n\tau)] = \mathbf{C}\mathbf{A}_2,$$

$$\Delta z(\tau) = \Delta a_{20} + \sum_{n=1}^{N_h} [\Delta a_{2n}\cos(n\tau) + \Delta b_{2n}\sin(n\tau)] = \mathbf{C}\Delta\mathbf{A}_2,$$

where

$$\mathbf{C} = [1 \quad \cos(\tau) \quad \cos(2\tau) \quad \ldots \quad \cos(N_h\tau) \quad \sin(\tau) \quad \sin(2\tau) \quad \ldots \quad \sin(N_h\tau)],$$

$$\mathbf{A}_s = \left[a_{s0} \quad a_{s1} \quad a_{s2} \quad \dots \quad a_{sN_h} \quad b_{s1} \quad b_{s2} \quad \dots \quad b_{sN_h}\right]^T,$$

$$\Delta\mathbf{A}_s = \left[\Delta a_{s0} \quad \Delta a_{s1} \quad \Delta a_{s2} \quad \dots \quad \Delta a_{sN_h} \quad \Delta b_{s1} \quad \Delta b_{s2} \quad \dots \quad \Delta b_{sN_h}\right]^T, (s = 1, 2).$$

By inserting relations Eq. (8) and Eq. (9) into Eq. (6) and Eq. (7) and neglecting the higher order terms including Δx_p^2 and Δz^2, linearised differential motion equations are obtained in the following form

$$\left(\frac{\Omega}{\omega_p}\right)^2\Delta\ddot{x}_p + \Lambda\Omega\Delta\dot{x}_p + \Delta x_p - \lambda\Omega\Delta\dot{z} - k\Delta z - 3Kz_0^2\Delta z \tag{10}$$

$$= -\left[\left(\frac{\Omega}{\omega_p}\right)^2\ddot{x}_{p0} + \Lambda\Omega\dot{x}_{p0} + x_{p0}\right] + \left[\lambda\Omega\dot{z}_0 + kz_0 + Kz_0^3\right] + Y_0(\sin(\tau) + \Lambda\Omega\cos(\tau)) + \Delta Y(\sin(\tau) + \Lambda\Omega\cos(\tau)),$$

and

$$\left(\frac{\Omega}{\omega_a}\right)^2\Delta\ddot{z} + \lambda\Omega\Delta\dot{z} + k\Delta z + 3Kz_0^2\Delta z + \left(\frac{\Omega}{\omega_a}\right)^2\Delta\ddot{x}_p \tag{11}$$

$$= -\left[\left(\frac{\Omega}{\omega_a}\right)^2\ddot{z}_0 + \lambda\Omega\dot{z}_0 + kz_0 + Kz_0^3\right] - \left[\left(\frac{\Omega}{\omega_a}\right)^2\ddot{x}_{p0}\right].$$

Then, the Galerkin procedure (i.e. orthogonality conditions for trigonometric functions [35]) is applied in order to eliminate τ as

$$< g(\tau), f(\tau) >= \frac{1}{2\pi}\int_0^{2\pi} f(\tau)g(\tau)d\tau = 0. \tag{12}$$

Applying the Galerkin procedure to the Eq. (10) and Eq. (11), yields

$$\int_0^{2\pi}\mathbf{C}^T\left[\left(\frac{\Omega}{\omega_p}\right)^2\ddot{\mathbf{C}} + \Lambda\Omega\dot{\mathbf{C}} + \mathbf{C}\right]d\tau\Delta\mathbf{A}_1 - \int_0^{2\pi}\mathbf{C}^T\left[\lambda\Omega\dot{\mathbf{C}} + k\mathbf{C} + 3Kz_0^2\mathbf{C}\right]d\tau\Delta\mathbf{A}_2 \tag{13}$$

$$= -\int_0^{2\pi}\mathbf{C}^T\left[\left(\frac{\Omega}{\omega_p}\right)^2\ddot{\mathbf{C}} + \Lambda\Omega\dot{\mathbf{C}} + \mathbf{C}\right]d\tau\mathbf{A}_1 + \int_0^{2\pi}\mathbf{C}^T\left[\lambda\Omega\dot{\mathbf{C}} + k\mathbf{C} + Kz_0^2\mathbf{C}\right]d\tau\mathbf{A}_2 +$$

$$+\int_0^{2\pi}\mathbf{C}^T[Y_0(\sin(\tau) + \Lambda\Omega\cos(\tau)) + \Delta Y(\sin(\tau) + \Lambda\Omega\cos(\tau))]d\tau,$$

$$\int_0^{2\pi}\mathbf{C}^T\left[\left(\frac{\Omega}{\omega_a}\right)^2\ddot{\mathbf{C}} + \lambda\Omega\dot{\mathbf{C}} + k\mathbf{C} + 3Kz_0^2\mathbf{C}\right]d\tau\Delta\mathbf{A}_2 + \int_0^{2\pi}\mathbf{C}^T\left[\left(\frac{\Omega}{\omega_a}\right)^2\ddot{\mathbf{C}}\right]d\tau\Delta\mathbf{A}_1 \tag{14}$$

$$= -\int_0^{2\pi}\mathbf{C}^T\left[\left(\frac{\Omega}{\omega_a}\right)^2\ddot{\mathbf{C}} + \lambda\Omega\dot{\mathbf{C}} + k\mathbf{C} + Kz_0^2\mathbf{C}\right]d\tau\mathbf{A}_2 - \int_0^{2\pi}\mathbf{C}^T\left[\left(\frac{\Omega}{\omega_a}\right)^2\ddot{\mathbf{C}}\right]d\tau\mathbf{A}_1.$$

which leads to the following system of algebraic equations

$$\begin{bmatrix}\mathbf{K}_{11} & \mathbf{K}_{12}\\ \mathbf{K}_{21} & \mathbf{K}_{22}\end{bmatrix}\begin{Bmatrix}\Delta\mathbf{A}_1\\ \Delta\mathbf{A}_2\end{Bmatrix} = \begin{Bmatrix}\mathbf{F}_1\\ \mathbf{0}\end{Bmatrix} + \begin{bmatrix}\mathbf{R}_{11} & \mathbf{R}_{12}\\ \mathbf{R}_{21} & \mathbf{R}_{22}\end{bmatrix}\begin{Bmatrix}\mathbf{A}_1\\ \mathbf{A}_2\end{Bmatrix} + \begin{Bmatrix}\mathbf{V}_1\\ \mathbf{0}\end{Bmatrix}\Delta Y. \tag{15}$$

The general form is given as

$$\mathbf{K}\Delta\mathbf{A} = \mathbf{R} + \mathbf{V}\Delta Y, \tag{16}$$

where

$$\mathbf{K} = \begin{bmatrix}\mathbf{K}_{11} & \mathbf{K}_{12}\\ \mathbf{K}_{21} & \mathbf{K}_{22}\end{bmatrix}, \quad \Delta\mathbf{A} = \begin{Bmatrix}\Delta\mathbf{A}_1\\ \Delta\mathbf{A}_2\end{Bmatrix}, \quad \mathbf{R} = \begin{Bmatrix}\mathbf{F}_1\\ \mathbf{0}\end{Bmatrix} + \begin{bmatrix}\mathbf{R}_{11} & \mathbf{R}_{12}\\ \mathbf{R}_{21} & \mathbf{R}_{22}\end{bmatrix}\begin{Bmatrix}\mathbf{A}_1\\ \mathbf{A}_2\end{Bmatrix}, \quad \mathbf{V} = \begin{Bmatrix}\mathbf{V}_1\\ \mathbf{0}\end{Bmatrix}.$$

where the matrices are defined as

$$\mathbf{K}_{11} = \int_0^{2\pi}\left\{\left(\frac{\Omega}{\omega_p}\right)^2\mathbf{C}^T\ddot{\mathbf{C}} + \Lambda\Omega\mathbf{C}^T\dot{\mathbf{C}} + \mathbf{C}^T\mathbf{C}\right\}d\tau, \tag{17}$$

$$\mathbf{K}_{12} = -\int_0^{2\pi}\left\{\lambda\Omega\mathbf{C}^T\dot{\mathbf{C}} + (k + 3\ Kz_0^2)\mathbf{C}^T\mathbf{C}\right\}d\tau,$$

$$\mathbf{K}_{21} = \int_0^{2\pi} \left\{ \left(\frac{\Omega}{\omega_a} \right)^2 \mathbf{C}^T \ddot{\mathbf{C}} \right\} d\tau,$$

$$\mathbf{K}_{22} = \int_0^{2\pi} \left\{ \left(\frac{\Omega}{\omega_a} \right)^2 \mathbf{C}^T \ddot{\mathbf{C}} + \lambda\Omega \mathbf{C}^T \dot{\mathbf{C}} + (k + 3\ Kz_0^2) \mathbf{C}^T \mathbf{C} \right\} d\tau,$$

$$\mathbf{F}_1 = \int_0^{2\pi} \left\{ Y_0 \mathbf{C}^T \sin(\tau) + \Lambda\Omega Y_0 \mathbf{C}^T \cos(\tau) \right\} d\tau,$$

$$\mathbf{V}_1 = \int_0^{2\pi} \left\{ \mathbf{C}^T \sin(\tau) + \Lambda\Omega \mathbf{C}^T \cos(\tau) \right\} d\tau,$$

$$\mathbf{R}_{11} = -\int_0^{2\pi} \left\{ \left(\frac{\Omega}{\omega_p} \right)^2 \mathbf{C}^T \ddot{\mathbf{C}} + \Lambda\Omega \mathbf{C}^T \dot{\mathbf{C}} + \mathbf{C}^T \mathbf{C} \right\} d\tau,$$

$$\mathbf{R}_{12} = \int_0^{2\pi} \left\{ \lambda\Omega \mathbf{C}^T \dot{\mathbf{C}} + (k + Kz_0^2) \mathbf{C}^T \mathbf{C} \right\} d\tau,$$

$$\mathbf{R}_{21} = -\int_0^{2\pi} \left\{ \left(\frac{\Omega}{\omega_a} \right)^2 \mathbf{C}^T \ddot{\mathbf{C}} \right\} d\tau,$$

$$\mathbf{R}_{22} = -\int_0^{2\pi} \left\{ \left(\frac{\Omega}{\omega_a} \right)^2 \mathbf{C}^T \ddot{\mathbf{C}} + \lambda\Omega \mathbf{C}^T \dot{\mathbf{C}} + (k + Kz_0^2) \mathbf{C}^T \mathbf{C} \right\} d\tau.$$

In order to analyse the frequency response, i.e. the effects of varying excitation frequency Ω on the vibration amplitude, $\Omega = \Omega_0 + \Delta\Omega$, $Y_0 \to Y$ and Eq. (8) are introduced into Eq. (6) and Eq. (7) to obtain a new system of algebraic equations as

$$\begin{bmatrix} \mathbf{K}_{11} & \mathbf{K}_{12} \\ \mathbf{K}_{21} & \mathbf{K}_{22} \end{bmatrix} \begin{Bmatrix} \Delta\mathbf{A}_1 \\ \Delta\mathbf{A}_2 \end{Bmatrix} = \begin{Bmatrix} \mathbf{F}_1 \\ \mathbf{0} \end{Bmatrix} + \begin{bmatrix} \mathbf{R}_{11} & \mathbf{R}_{12} \\ \mathbf{R}_{21} & \mathbf{R}_{22} \end{bmatrix} \begin{Bmatrix} \Delta\mathbf{A}_1 \\ \Delta\mathbf{A}_2 \end{Bmatrix} + \begin{Bmatrix} \mathbf{V}_1 \\ \mathbf{V}_2 \end{Bmatrix} \Delta\Omega, \tag{18}$$

where the only difference with respect to Eq. (15) lies in the vector that multiplies $\Delta\Omega$, which is given as

$$\mathbf{V}_1 = \int_0^{2\pi} \left\{ \Lambda Y \mathbf{C}^T \cos(\tau) \right\} d\tau - \int_0^{2\pi} \left\{ 2\frac{\Omega_0}{\omega_p^2} \mathbf{C}^T \ddot{\mathbf{C}} + \Lambda \mathbf{C}^T \dot{\mathbf{C}} \right\} d\tau \mathbf{A}_1 + \int_0^{2\pi} \left\{ \lambda \mathbf{C}^T \dot{\mathbf{C}} \right\} d\tau \mathbf{A}_2, \tag{19}$$

$$\mathbf{V}_2 = -\int_0^{2\pi} \left\{ 2\frac{\Omega_0}{\omega_a^2} \mathbf{C}^T \ddot{\mathbf{C}} \right\} d\tau \mathbf{A}_1 - \int_0^{2\pi} \left\{ 2\frac{\Omega_0}{\omega_a^2} \mathbf{C}^T \ddot{\mathbf{C}} + \lambda \mathbf{C}^T \dot{\mathbf{C}} \right\} d\tau \mathbf{A}_2.$$

It should be noted that Eq. (15) and Eq. (18) are systems of linear algebraic equations in terms of the unknown increments of amplitudes ΔA_s, whose solution can be found by using the Newton - Raphson iterative procedures. Here, the solution procedure is divided into two main steps. First, the initial values of A_{s0}, Ω_0 or Y_0 in Eq. (15) or Eq. (18) are assumed in such a manner that the tangent stiffness matrix $\mathbf{K}$ is not singular. Second, by using the iterative Newton - Raphson method, relations Eq. (15) and Eq. (18) are solved, where the results for ΔA_s are obtained iteratively by solving the $\Delta A = \mathbf{K}^{-1}\mathbf{R}$ until the residue Euclidian norm $\|\mathbf{R}\|$ is smaller than the pre-set tolerance. Here, the norm of the residuum vector is adopted as $\|\mathbf{R}\| \leq 10^{-9}$. In every iteration there is $\mathbf{A}_s^{p+1} = \mathbf{A}_s^p + \Delta\mathbf{A}_s^{p+1}$ for the fixed value of Ω_0 or Y_0. In that case, the corrective vector term $\mathbf{R}$ tends to zero when the values of $x_{p0}(\tau)$ and $z_0(\tau)$ tend to exact solutions. It is important to note that the matrices and vectors given in the previous relations are derived in analytical form (e.g. using the software Wolfram Mathematica or MAPLE), which saves a significant amount of time for the calculation of the incremental solution.

4. Stability of the periodic solution - Floquet theory

After finding the periodic solution in the form of Fourier series given in Eq. (9), the stability of thus obtained solution can be investigated by introducing a methodology based on the Floquet theory [31,32]. By using the Floquet theory in $\mathbb{R}^N$ for the system of nonlinear differential equations, the general form can be written as

$$\mathbf{W}(\ddot{\mathbf{y}}, \dot{\mathbf{y}}, \mathbf{y}, Y, \tau) = \mathbf{0}, \tag{20}$$

where $\mathbf{y} = [y_1(\tau),\ y_2(\tau), \ldots y_N(\tau)]$ is the N - dimensional displacement vector and $\dot{\mathbf{y}} = d\mathbf{y}/d\tau$. By inserting small perturbations $\Delta\mathbf{y}(\tau)$ in a neighbourhood of the periodic solution $\mathbf{y}_0(\tau)$, i.e. by letting

$$\mathbf{y} = \mathbf{y}_0 + \Delta\mathbf{y}(\tau), \tag{21}$$

the stability of periodic solutions can be analysed by introducing the linearised system of differential equations with variable coefficients in terms of small perturbations $\Delta\mathbf{y}(\tau)$. Introducing Eq. (21) into the system of Eq. (20), after linearisation we obtain the system of linear differential equations with time periodic coefficients as

$$\left(\frac{\partial \mathbf{W}}{\partial \ddot{\mathbf{y}}}\right)_0 \Delta\ddot{\mathbf{y}}(\tau) + \left(\frac{\partial \mathbf{W}}{\partial \dot{\mathbf{y}}}\right)_0 \Delta\dot{\mathbf{y}}(\tau) + \left(\frac{\partial \mathbf{W}}{\partial \mathbf{y}}\right)_0 \Delta\mathbf{y}(\tau) = \mathbf{0}, \tag{22}$$

where $\mathbf{y}_0(\tau) = [x_p(\tau), z(\tau)]^T$ is the periodic solution determined by the IHB procedures. It should be noted that Eq. (22) represents the system of perturbed equations in the vicinity of the known periodic solutions $\mathbf{y}_0(\tau)$. The stability characteristics of the known periodic solutions are found through the multi-variable Floquet theory. Transformation of Eq. (22) into the state-space form yields

$$\frac{d\mathbf{Y}}{d\tau} = \mathbf{P}(\tau)\mathbf{Y}, \tag{23}$$

where $\mathbf{Y}(\tau) = [\Delta\mathbf{y}, \Delta\dot{\mathbf{y}}]^T$ and $\mathbf{P}(\tau)$ denotes the periodic matrix with the period T.

The stability criteria based on the Floquet theory [28,36] for finding the periodic solutions of the system of equations Eq. (6) and Eq. (7) is based on determination of the Floquet multipliers (i.e. determination of eigenvalues of the monodromy matrix $\mathbf{M}$ [28,31]). In the case when all values of Floquet multipliers are located inside the unit circle centred at the origin of the complex plane, the periodic solutions are stable or asymptotically stable. In contrast to this, when Floquet multipliers lie outside of the unit circle the periodic solutions are unstable [36]. Depending on a location where the Floquet multipliers or a pair of complex conjugate multipliers crosses the unit circle, one can detect different bifurcation points such as Hopf, Saddle-node, and period of doubling bifurcations [36,37]. In the following, the so-called Hsu procedure for the numerical determination of Floquet multipliers [28,30,38] is adopted. It is assumed that the period $T = 2\pi$ of $y_0(\tau)$ is divided into N_k sub-intervals, in which the k-th interval is $\Delta_k = \tau_k - \tau_{k-1}$ for $\tau_k = kT/N_k$. Moreover, $P(\tau)$ is the continuous periodic matrix with respect to τ, such that it can be replaced by a constant matrix in the k-th interval for the case when N_k is chosen to be sufficiently large, as

$$\mathbf{P}_k = \frac{1}{\Delta_k}\int_{\tau_{k-1}}^{\tau_k} \mathbf{P}(\tau)d\tau, \tag{24}$$

where the transition matrix can take the following form

$$\mathbf{M} = \prod_{i=1}^{N_k} e^{\mathbf{P}_i\Delta_i} = \prod_{i=1}^{N_k}\left(\mathbf{I} + \sum_{j=1}^{N_j}\frac{(\mathbf{P}_i\Delta_i)^j}{j!}\right), \tag{25}$$

in which N_j denotes the number of terms in the approximation of the constant matrix $\mathbf{P}_k$. From the transition matrix $\mathbf{M}$ one can obtain Floquet multipliers as eigenvalues of Eq. (25) in the form

$$\det(\mathbf{M} - \sigma\mathbf{I}) = 0. \tag{26}$$

For the presented mathematical model given in Eq. (6) and Eq. (7), by considering $z = x_a - x_p$, the periodic matrix $\mathbf{P}(\tau)$ has the following form

$$\mathbf{P}(\tau) = -\begin{bmatrix} 0 & -1 & 0 & 0 \\ \frac{C_1}{A_1} & \frac{B_1}{A_1} & \frac{E_1}{A_1} & \frac{D_1}{A_1} \\ 0 & 0 & 0 & -1 \\ \frac{E_2}{A_2} & \frac{D_2}{A_2} & \frac{C_2}{A_2} & \frac{B_2}{A_2} \end{bmatrix}, \tag{27}$$

where coefficients are given as

$$A_1 = \left(\frac{\Omega}{\omega_p}\right)^2, \quad B_1 = \Omega(\Lambda + \lambda), \quad C_1 = 1 + k + 3\ K(x_{a0}^2 - 2x_{a0}x_{p0} + x_{p0}^2),$$

$$D_1 = -\Omega\lambda, \quad E_1 = -k - 3\ K(x_{a0}^2 - 2x_{a0}x_{p0} + x_{p0}^2),$$

$$A_2 = \left(\frac{\Omega}{\omega_a}\right)^2, \quad B_2 = \Omega\lambda, \quad C_2 = k + 3\ K(x_{a0}^2 - 2x_{a0}x_{p0} + x_{p0}^2),$$

$$D_2 = -\Omega\lambda, \quad E_2 = -k - 3\ K(x_{a0}^2 - 2x_{a0}x_{p0} + x_{p0}^2).$$

The terms $x_{a0}(\tau)$ and $x_{p0}(\tau)$ are determined in the form of Fourier's series. According to the convergence study based on the transition matrix obtained by the Hsu's procedure [38,39] the following values are adopted $N_k = 5000$ and $N_j = 5$.

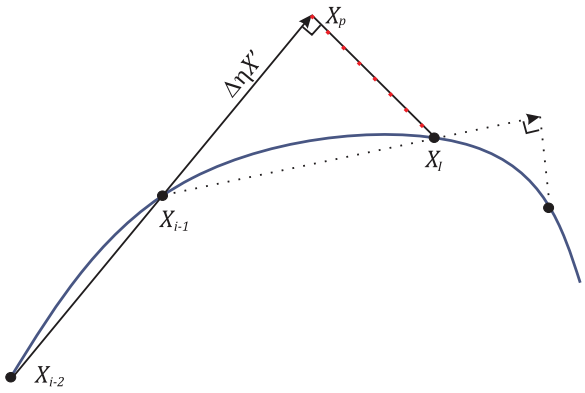

Fig. 2. The illustration of an arc-length continuation scheme for a response curve.

5. Continuation method in combination with IHB

To trace the frequency-amplitude or response amplitude - base amplitude curves, the solution procedure starts from an arbitrary initial vibration state (it can be started from some linear solution far away from the resonance state or with a small value of excitation force amplitude). Then, point-to-point calculation is performed by using the ΔY incremental equation Eq. (15) or $\Delta\Omega$ incremental equation Eq. (18) to obtain the corresponding response curves, as shown in [40]. However, this solution procedure can fail if some limit points (such as turning points) are encountered or solution curve forms a loop (when the curve cuts itself). In such cases, standard incremental relations formed directly from the IHB methodology do not yield satisfying results. In order to trace response curves in the entire frequency or force amplitude range, and to eliminate failures due to the limit points, one may use the arc-length continuation techniques in combination with the IHB method. Here, a methodology known as the predictor-corrector method based on the arc-length continuation [30,36] is employed.

Fig. 2 shows the scheme how the arc-length continuation method works when tracing the periodic solution response curves. In order to trace the response curve, two initial points $(\mathbf{X}_{i-2}, \mathbf{X}_{i-1})$ should be first determined by the IHB method and then by introducing the arc-length continuation parameter η one can find a slope in the following form

$$\mathbf{X}' = \frac{\mathbf{X}_{i-1} - \mathbf{X}_{i-2}}{\|\mathbf{X}_{i-1} - \mathbf{X}_{i-2}\|}, \tag{28}$$

where $\mathbf{X}$ is the vector $\mathbf{X} = [\mathbf{A}, Y]^T$ or $X = [\mathbf{A}, \Omega]^T$, depending on the response curve, which is necessary to trace the frequency-amplitude or response amplitude - base amplitude curves. The first predicted solution of the next point X_i on the solution branch is given by the formula

$$\mathbf{X}_p = \mathbf{X}_{i-1} - \Delta\eta\mathbf{X}', \tag{29}$$

Now, a corrected solution can be found by using the Newton - Raphson method, where the starting point is the first predicted solution of X_i on the tracing branch (i.e. X_p). Before that step, one should extend the system given in equations Eq. (15) or Eq. (18) by an augmented equation

$$g(\mathbf{X}) - \eta = 0. \tag{30}$$

Based on the methodology from [28,29,37], the quadratic form of the pseudo arc-length method and function $g(\mathbf{X}) = \mathbf{X}^T\mathbf{X}$ are adopted, where the incremental relation for Eq. (30) is given as

$$\frac{\partial g}{\partial \mathbf{A}^T}\Delta\mathbf{A} + \frac{\partial g}{\partial Y}\Delta Y + g - \eta - \Delta\eta = 0, \tag{31}$$

By considering the extended system, i.e. combining Eq. (18) and Eq. (31), the system of incremental equations for tracing the response amplitude - base amplitude curves can be obtained as

$$\begin{bmatrix} \mathbf{K}_{11} & \mathbf{K}_{12} & -\mathbf{V}_1 \\ \mathbf{K}_{21} & \mathbf{K}_{22} & -\mathbf{V}_2 \\ \left\{\frac{\partial g}{\partial \mathbf{A}_1}\right\}^T & \left\{\frac{\partial g}{\partial \mathbf{A}_2}\right\}^T & \frac{\partial g}{\partial Y} \end{bmatrix} \begin{Bmatrix} \Delta\mathbf{A}_1 \\ \Delta\mathbf{A}_2 \\ \Delta Y \end{Bmatrix} = \begin{Bmatrix} \mathbf{R}_1 \\ \Delta\mathbf{R}_2 \\ \Delta\eta - g \end{Bmatrix}, \tag{32}$$

where

$$\mathbf{R}_1 = \mathbf{F}_1 + [\mathbf{R}_{11}]\mathbf{A}_1 + [\mathbf{R}_{12}]\mathbf{A}_2,$$

$$\mathbf{R}_2 = [\mathbf{R}_{21}]\mathbf{A}_1 + [\mathbf{R}_{22}]\mathbf{A}_2.$$

For tracing the frequency-amplitude response curve, the same methodology can be employed by combining the Eq. (18) and Eq. (31) and adopting $\mathbf{X} = [\mathbf{A}, \Omega]^T$.

Table 1
Material parameters of the presented nonlinear NES-EH model.

Parameter	Value
m_p	0.917 kg
m_a	0.061 kg
k_p	4870 N/m
c_p	1.3747 Ns/m
k_a	50.81 N/m
k_n	9.539×10^7 N/m^3
c_{am}	0.17 Ns/m
k_t	5.03 Tm
Y	8×10^{-5}m
R_{coil}	6 Ω

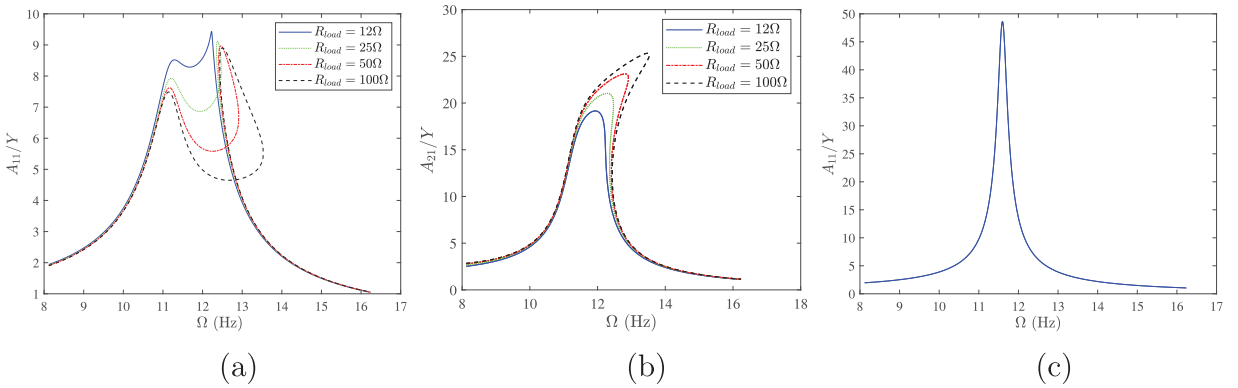

Fig. 3. The frequency-amplitude response curve for different values of the resistance load R_{load}, response amplitude ratios (a) A_{11}/Y and (b) A_{21}/Y; (c) The frequency-response diagram of the primary structure A_{11}/Y without the NES mass.

6. Parametric study

This section is divided into two main parts. In the first part, a comparative study of the results obtained in the present work against the results given by Kremer and Liu [23] is presented. Based on the IHB and continuation methodology described in previous sections, the nonlinear dynamic behaviour of the proposed NES-EH model is studied. Special attention is devoted to investigation of the periodic responses in the form of frequency-amplitude curves. The periodic orbits obtained by the IHB method are validated with the results obtained by the Runge-Kutta method (ode45 - MATLAB). In the second part of this section, the influence of the resistance load R_{load}, nonlinear stiffness parameter K and excitation frequency Ω on the nonlinear response amplitude - base amplitude curves is analysed. The presented analysis of the effect of change in the amplitude of external base excitation for fixed values of excitation frequency gives a more complete picture of working conditions of the proposed model, which could be useful in design procedures of NES-EH devices. Moreover, time response diagrams show the effect of structural parameters and different excitation frequencies on the energy localization and harvesting performance. In should be noted that all the computations and program codes are developed in the MATLAB environment.

6.1. Validation study

The validation study is performed to show the accuracy of the presented semi-analytical methodology based on the IHB and continuation methods for tracing the response curves. Material parameters of NES-EH model are given in Table 1,

The values of the load resistance are adopted as $R_{load} = 12,\ 25,\ 50,\ 100\ \Omega$. Based on the convergence study given in numerous papers [31,35,41], $N_h = 6$ terms are adopted in the Fourier series. Fig. 3 shows the bifurcation diagram that represents the frequency response for both displacements of the NES-EH system $x_p(\tau)$ and $z(\tau)$, which are determined in terms of the Fourier series defined by

$$x_p(\tau) = A_{10} + A_{11}\cos(\tau + \phi_{11}) + A_{12}\cos(2\tau + \phi_{12}) + \ldots, \tag{33}$$

$$z(\tau) = A_{20} + A_{21}\cos(\tau + \phi_{21}) + A_{22}\cos(2\tau + \phi_{22}) + \ldots,$$

where

$$A_{s0} = a_{s0}, \quad A_{sn} = \sqrt{a_{sn}^2 + b_{sn}^2}, \quad \phi_{sn} = \tan^{-1}(b_{sn}/a_{sn}), \quad (s = 1, 2; \quad n = 1, 2 \ldots, 6).$$

The response diagrams show the influence of resistance load R_{load} when the excitation frequency Ω varies in the range $8-16$ *Hz*. The ordinate axis represents the amplitude ratios A_{11}/Y and A_{21}/Y for the first harmonic of both displacements $x_p(\tau)$ and $z(\tau)$, while the abscissa shows the excitation frequency Ω. The presented NES-EH model is a two-degree of freedom system with two natural frequencies that are determined by neglecting the nonlinear and damping terms in Eq. (9) and Eq. (15), which yields

$$\lambda_{1/2}=\sqrt{\frac{k\omega_p^2+k\omega_a^2+\omega_p^2}{2}\pm\sqrt{\frac{1}{4}(k\omega_p^2+k\omega_a^2+\omega_p^2)^2-k\omega_p^2\omega_a^2}}, \tag{34}$$

where the first natural frequency corresponds to $f_1=\frac{\lambda_1}{2\pi}=4.565$ Hz and it is close to the natural frequency of the attached substructure $f_a=4.593$ Hz. The second natural frequency $f_2=\frac{\lambda_2}{2\pi}=11.669$ Hz is close to the frequency of a primary structure $f_p=11.598$ Hz.

The response diagrams given in Fig. 3 show the dependency between the amplitude and the frequency for the primary structure system both with (Fig. 3(a) and (b)), and without the additional NES device (Fig. 3(c)). As stated before, the primary structure with additional NES device is equivalent to NES-EH system. By comparing the responses of these two systems, a significant reduction in response amplitude of the system with NES device can be observed, demonstrating the importance of NES mechanism in vibration suppression. Despite the fact that stability analysis is not performed for these examples, tracing the response curves can provide many useful insights into the nonlinear behaviour and periodic responses of the observed systems.

In Fig. 3(a), one can observe almost linear change of the frequency - amplitude response curve for an increase of the excitation frequency Ω until the value is close to 11 *Hz*, when the first resonant peak appears. A further increase of the excitation frequency Ω leads to almost linear change of the response curve until the excitation frequency reaches the value close to 12.5 *Hz*, when the response curve forms a loop. This region of coexisting periodic responses within the loop widens with an increase of the value of the resistance load R_{load}. It should be noted that the second resonant peak appears on the response curve A_{11} at small values of the resistance load. From the physical point of view, such nonlinear response of the amplitude A_{11} is caused by adding the nonlinear attachment to the linear primary structure, which is explained in the previous studies [9,42]. Moreover, the response amplitude A_{11} shows a significant dependence on the resistance load R_{load} such that an increase of parameter R_{load} leads to a decrease of the overall system's damping. In general, for an increase of the resistance load R_{load} nonlinear phenomena becomes more prominent in the frequency-amplitude response diagrams.

The second frequency response shows the amplitude ratio A_{22}/Y with the hardening spring type nonlinearity, which implies the jump phenomena. It can be seen that for higher values of the resistance load R_{load} the hardening nonlinearity is more emphasized, causing the response curve to bend to the right. However, it can be observed that at lower values of the resistance load R_{load} the response amplitude ratio A_{22}/Y changes almost linearly.

Finally, comparison of the response amplitude ratio A_{11}/Y obtained for the primary structure without NES against the response amplitudes of NES-EH model in Fig. 3(c) reveals a significant decrease of the response amplitude due to the attached NES device. Comparison of the response amplitudes obtained by the IHB and the continuation method given in Fig. 3 and the results from [23] obtained by combining the mixed multiple scales/harmonic balance method with MATCONT software [43] shows a fine agreement.

It should be noted that the periodic time response and phase space diagrams determined by using the IHB methods for both displacements, $x_p(\tau)$ and $x_a(\tau)$, are validated against the numerical results obtained by the direct numerical integration (NI) in Matlab (ode 45), Fig. 4. Values of parameters used in these calculations are given in Table 1, except for the values of excitation frequency and resistance load that are adopted as $\Omega=\omega_p$ and $R_{load}=25\ \ \Omega$. One can notice a very good match between the compared results. Advantages of the IHB method with respect to the perturbation and NI methods are demonstrated by finding the periodic responses for the system with strong nonlinearity without introduction of the small scale parameter (unlike in the perturbation methods) and obtaining the semi-analytical results in terms of the Fourier coefficients.

6.2. The base amplitude force response of the NES-EH system

In the following, a nonlinear dynamic behaviour of the NES-EH system within the framework of the IHB and continuation methods is investigated. The obtained results are given in the form of response amplitude - base amplitude response curves. The material parameters adopted in this numerical investigation are given in Table 1, where the following values of resistance loads $R_{load}=12,\ \ 25,\ \ 50,\ \ 100\ \ \Omega$ and excitation frequency $\Omega=0.7\ \ \omega_p,\ \ 0.9\ \ \omega_p,\ \ 1.1\ \ \omega_p$ are adopted. In order to investigate the influence of the nonlinear stiffness parameter K and NES on the response amplitudes, the following values of $0.1\ \ K$, $0.4\ \ K$ and $0.8\ \ K$ are adopted in this section. Any further change of system parameters is additionally mentioned within the discussion of the obtained results.

6.2.1. Base amplitude force response diagrams for amplitudes A_{11} *and* A_{21}

Figs. 5–9 shows the response amplitude - Base amplitude curves A_{11} and A_{21} obtained for the displacements $x_p(\tau)$ and $z(\tau)$ of the NES-EH system. The response amplitudes are determined in terms of Fourier series from Eq. (33). The presented results show the effects of the resistance load R_{load} and nonlinear stiffness parameter K on the response amplitude - base

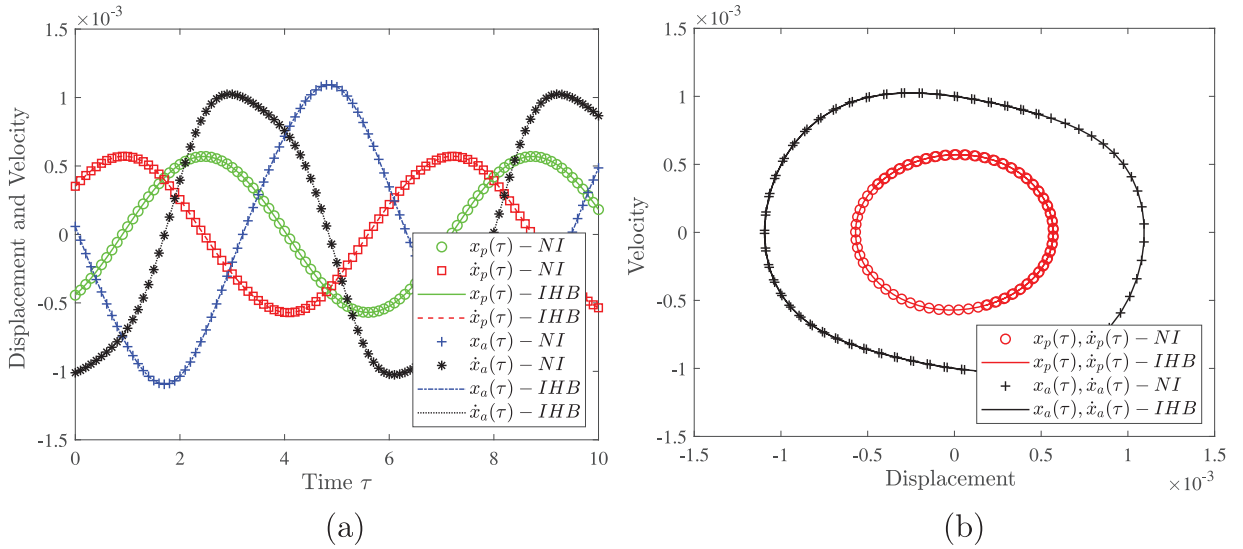

Fig. 4. The comparison of the response amplitudes obtained by the incremental harmonic balance (IHB) method and direct numerical integration (NI); (a) time response and (b) the corresponding phase space. The results obtained by the IHB method are represented by solid lines and results obtained by direct NI are represented by discrete markers.

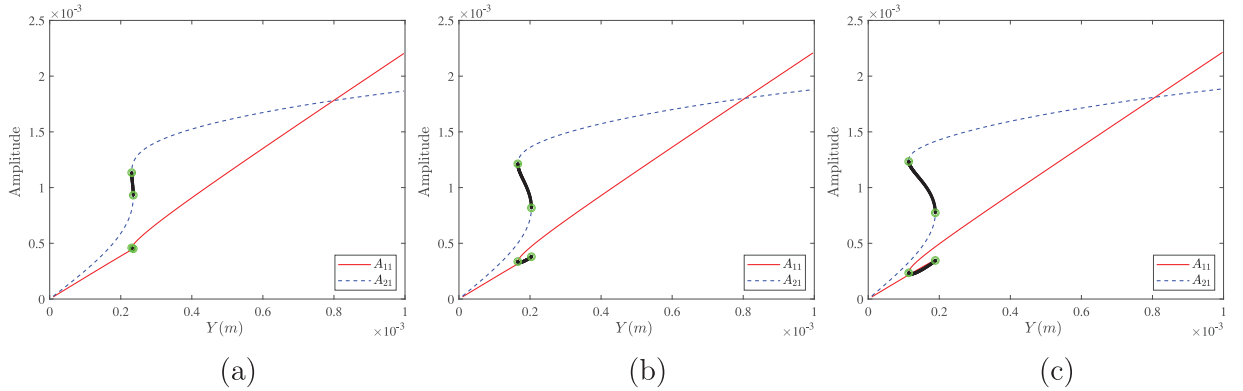

Fig. 5. The response amplitude - base amplitude curves for different values of the resistance load R_{load}; a) $R_{load} = 12\ \ \Omega$, b) $R_{load} = 25\ \ \Omega$, c) $R_{load} = 50\ \ \Omega$, where $\Omega = 0.7\ \ \omega_p$. The solid red line represents the response amplitude A_{11}, and the dashed blue line is the response amplitude A_{21}. The black points represent unstable branches of the periodic response.

amplitude curves for changes of external base excitation amplitude Y in the range $0 - 0.001\ \ m$. The ordinate axis represents the amplitudes A_{11} and A_{21} while the abscissa shows the base excitation amplitude Y. From the practical point of view, two cases of excitation frequency $\Omega = 0.7\ \ \omega_p$ and $\Omega = 1.1\ \ \omega_p$ are analysed, i.e. before and after the resonant state. In the case when the external excitation frequency is close to the natural frequency ω_p, the beating phenomenon is detected. Here, this state can be observed in the case when the excitation frequency takes the following value $\Omega = 1.1\ \ \omega_p$. A significant difference in the response curves of the NES-EH system obtained before and after passing through the resonant state can be observed, which will be explained in detail in the following text.

Fig. 5 shows the response amplitude - base amplitude of the NES-EH system for the excitation frequency $\Omega = 0.7\ \ \omega_p$ and load resistance in the range $R_{load} = 12 - 50\ \ \Omega$. Other material parameters are given in Table 1. One can notice that two response amplitude curves A_{11} and A_{21} show different dynamical behaviour, where in the response curve for A_{21} one can observe a "hysteresis phenomenon" with coexisting multiple periodic solutions. On the other hand, in the response curve A_{11} one can observe formation of a loop due to NES attachment [9]. An increase of the amplitude of external base excitation Y, starting from some small value $(10^{-5}m)$ leads to an increase of both amplitudes A_{11} and A_{21} until Y reaches some value around $Y = 0.22 \times\ \ 10^{-3}\ \ m$. Here, periodic solution loses its stability due to the appearance of saddle-node bifurcation (double green circle). This instability is detected by the calculation of Floquet multipliers, where at least one of them crosses the unit circle in the complex plane in $+1$ direction. Fig. 6 shows how Floquet multiplies crossing the unit circle in the complex plane in $+1$ direction are determined for the case given in Fig. 5(c). It should be noted that the unstable branch of the periodic solutions is located between two saddle-node bifurcation points (double green circles),

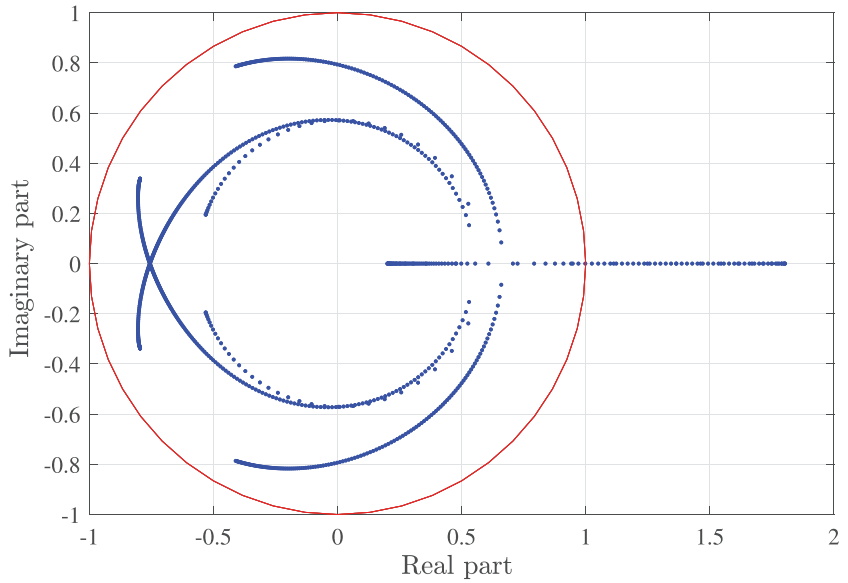

Fig. 6. The Floquet multipliers crossing the unit circle in the complex plane in +1 direction, determined for the case given on Fig. 5(c), where the $R_{load} = 50\ \Omega$. The solid red line represents the unit circle in the complex plane, and the blue points are the Floquet multipliers.

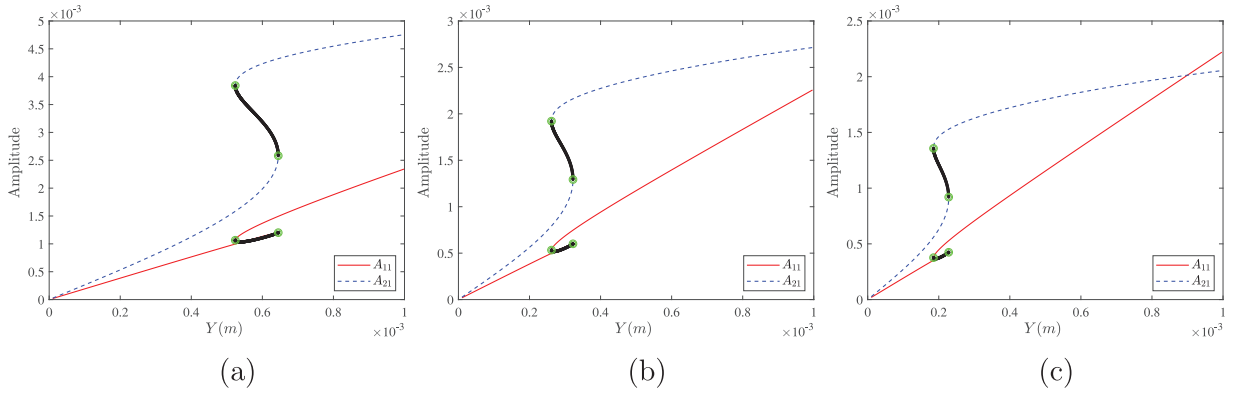

Fig. 7. The response amplitude - base amplitude curves for different values of the nonlinear stiffness parameter K; a) $0.1K$, b) $0.4K$, c) $0.8K$, where $\Omega = 0.7\ \omega_p$ and $R_{load} = 25\ \Omega$. The solid red line represents the response amplitude A_{11}, and the dashed blue line is the response amplitude A_{21}. The black points represent unstable branches of the periodic response.

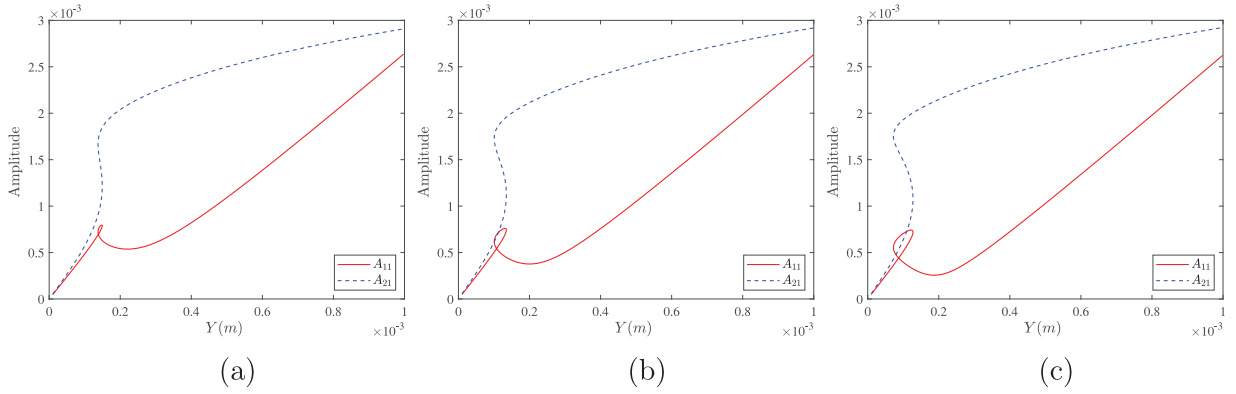

Fig. 8. The response amplitude - base amplitude curves for different values of the resistance load R_{load}; a) $R_{load} = 12\ \Omega$, b) $R_{load} = 25\ \Omega$, c) $R_{load} = 50\ \Omega$, where $\Omega = 1.1\ \omega_p$. The solid red line represents the response amplitude A_{11}, and the dashed blue line is the response amplitude A_{21}.

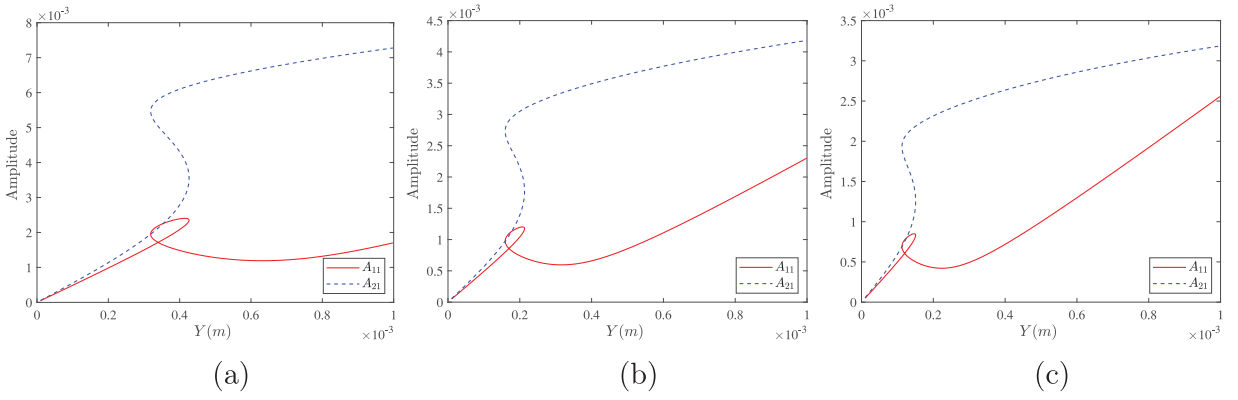

Fig. 9. The response amplitude - base amplitude curves for different values of the nonlinear stiffness parameter K; a) $0.1K$, b) $0.4K$, c) $0.8K$, where $\Omega = 1.1\ \omega_p$ and $R_{load} = 25\ \Omega$. The solid red line represents the response amplitude A_{11}, and the dashed blue line is the response amplitude A_{21}.

as shown by both response amplitudes. Further increase of Y, leads to an increase of both response amplitudes until the value of $Y = 1 \times 10^{-3}\ m$ is reached. In addition, by comparing the response amplitudes obtained for different values of the resistance load R_{load} in the range 12 - 50 Ω, it can be seen that an increase of the value of resistance load amplifies the nonlinear behaviour of the system. One can observe that reduction of the electric damping leads to higher vibration amplitudes of the system and therefore larger branches of unstable periodic response, which is attributed to direct relation between the resistance load and the electric damping c_e.

In order to investigate the effect of NES on the dynamic behaviour of the proposed NES-EH system, the response amplitude - base amplitude diagrams are traced for different values of the nonlinear stiffness parameter K and shown in Fig. 7. It can be observed that an increase of the nonlinear stiffness parameter K leads to a considerable decrease of the response amplitudes A_{11} and A_{21}. Here, an increase of the amplitude of external base excitation Y leads to an increase of both amplitudes A_{11} and A_{21} until Y reaches the value of approximately $Y = 0.62 \times 10^{-3}\ m$, where the periodic solution loses its stability due to the appearance of a saddle-node bifurcation (double green circle). It can be noticed that for an increase of the nonlinear stiffness parameter, the unstable branch of the periodic response is shifted to the left hand side. As expected, an increase of the nonlinear stiffness parameter leads to a reduction of the unstable branch of the periodic response.

For an increase in the external excitation frequency ratio Ω/ω_p the system passes through a resonant state, while for the fixed value of $\Omega/\omega_p = 1.1$, which is close to the resonant frequency, the system shows an interesting nonlinear behaviour that is known from the literature as the beating phenomenon. Special attention is devoted to this state of the system in the next section, showing the energy transfer from the primary structure to the NES device when the system is excited with the frequency close to the resonant one. The nonlinear dynamic behaviour of the NES-EH system excited by the frequency near the resonant one is presented in Figs. 8 and 9. The obtained response amplitude - base amplitude diagrams for higher values of excitation frequency are traced for different values of resistance load $R_{load} = 12,\ 25,\ 100\ \Omega$ and nonlinear stiffness parameters K. One can observe a similar nonlinear properties of the response amplitudes, where the traced curve A_{11} makes a loop while the curve A_{21} demonstrates the "hysteresis phenomenon". One can notice the coexisting multiple periodic solutions for both response amplitudes and similar range of values of the amplitude of excitation force Y. However, comparing the values of excitation frequency far from ($\Omega/\omega_p = 0.7$), and near the resonance frequency ($\Omega/\omega_p = 1.1$), one can notice significantly higher values of the response amplitudes near the resonance state. On the other hand, the nonlinear behaviour causing the three coexisting periodic solutions appears at smaller values of the external force amplitude Fig. 8, which are detected near $Y = 0.1 \times 10^{-3}$. Fig. 9 shows that the response amplitudes are also influenced by the changes of the nonlinear stiffness parameter, where loops are shifted to the left for an increase of K. For practical applications of the proposed nonlinear NES-EH system it is important to note that values of the response amplitude A_{11} are significantly smaller then the response amplitude A_{21} for all values of the amplitude of excitation load Y. This is especially obvious at higher values of excitation frequency $\Omega = 1.1\ \omega_p$. One of the main future tasks will be to find the optimal values of the nonlinear stiffness parameter and the corresponding mechanical and electrical damping in order to extend the vibration attenuation capabilities of the proposed NES-EH system.

6.2.2. The voltage responses curves

Figs. 10 and 11 illustrate the estimated voltage across the load resistor amplitude A_{31} of the proposed NES-EH model for different values of the resistance load $R_{load} = 12, 25, 50, 100\ \Omega$, nonlinear stiffness parameter $0.1K$, $0.4K$ and $0.8K$, and values of the excitation frequency $\Omega = (0.7,\ 0.9,\ 1.1)\ \omega_p$. In [24], the authors defined the amount of harvested energy as a summation of the power dissipated by the load resistor over a time period T. According to this definition, the voltage across the resistor given in Eq. (7) is used for tracing the corresponding response curves of voltage amplitude A_{31} for different values of Y. The amplitude A_{31} is defined in a similar way as it has been done for response amplitudes A_{11} and A_{21}, shown in Eq. (33). By increasing the amplitude of base excitation Y, the values of the response amplitude A_{31} linearly increase

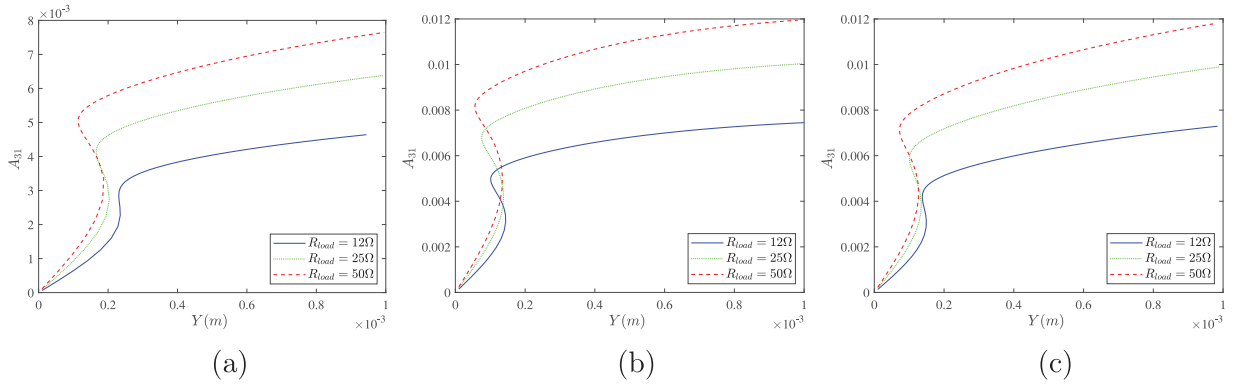

Fig. 10. The voltage response curves, for different values of the resistance load $R_{load} = 12,\ 25,\ 50\ \Omega$, and the excitation frequency Ω given, (a) $\Omega = 0.7\ \ \omega_p$, (b) $\Omega = 0.9\ \ \omega_p$, (c) $\Omega = 1.1\ \ \omega_p$.

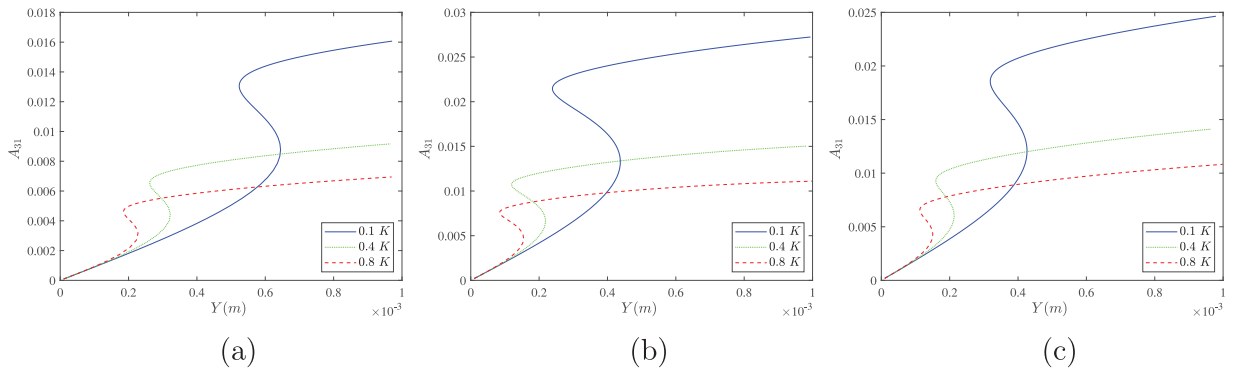

Fig. 11. The voltage response curve, for different values of the nonlinear stiffness parameter $0.1K$, $0.4K$ and $0.8K$, and the excitation frequency Ω given, (a) $\Omega = 0.7\ \ \omega_p$, (b) $\Omega = 0.9\ \ \omega_p$, (c) $\Omega = 1.1\ \ \omega_p$.

until they reach the point where the periodic response loses its stability, which leads to the appearance of the jump-up phenomenon. This process is known as forward force sweeping. Now, if sweeping starts from higher values of the amplitude of excitation force and goes backwards, the response amplitude A_{31} will decrease until the point where the periodic solution loses its stability leading to the jump-down effect. Moreover, this sweeping process in forward and backward direction creates a "hysteresis-loop" or a "hysteresis-phenomenon", as stated in the above examples. Moreover, up to three coexisting periodic solutions can be observed, corresponding to stable, unstable and again stable branches of the periodic responses in the range where hysteresis loop appears. From the practical viewpoint, especially for energy harvesting application, the range of values of the excitation amplitude Y with coexisting multiple responses is important for simultaneous output voltage generation and vibration suppression by the NES-EH system.

By comparing the periodic responses obtained for different values of the load resistance R_{load} it can be noticed that an increase of the parameter R_{load} leads to higher values of the response amplitude A_{31}, Fig. 10. The physical explanation of this phenomenon is attributed to the relationship with the electrical damping c_e, where an increase the resistance load R_{load} reduces the values of the electrical damping. Based on this fact, it can be concluded that reducing the overall damping in the system leads to higher values of the response amplitudes, which is useful for energy harvesting application. On the other hand, an increase of the nonlinear stiffness parameter decreases the response amplitude A_{31} for all values of excitation frequency, Fig. 11. From the physical point of view, this means that an increase of the nonlinear stiffness parameter leads to an increase of the overall stiffness of the system, while the response amplitude A_{31} decreases. Comparing the response amplitudes obtained for the cases when the excitation frequency is far from ($\Omega/\omega_p = .7$), and close to the resonant frequency ($\Omega/\omega_p = .9$ and $\Omega/\omega_p = 1.1$), it is evident that the amplitude A_{31} has higher values near the resonant state. This could be of practical significance in design procedures of NES-EH devices by pointing out the adequate values of material parameters of the system and excitation frequency, which can reduce the unstable branches and eliminate jumps in estimated voltage responses.

6.3. Time responses of the NES-EH system

In order to investigate performances of the proposed NES-EH device in vibration suppression and energy harvesting application, the time responses for displacements $x_p(t)$, $x_a(t)$ and output voltage $v(t)$ diagrams are investigated in this subsection.

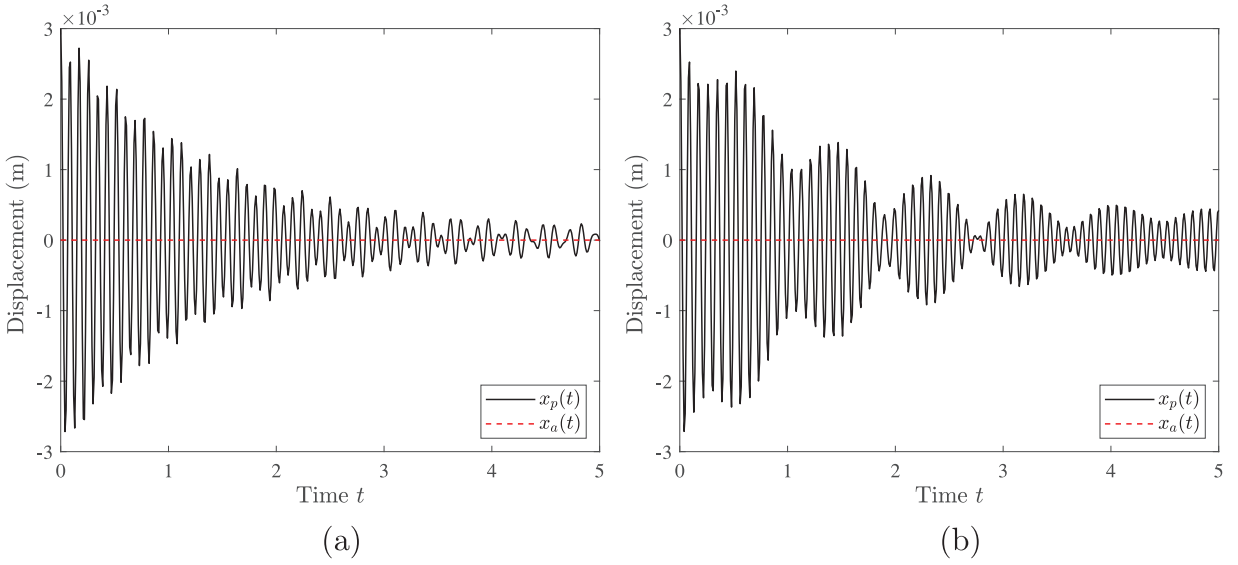

Fig. 12. The time responses of the primary structure for different excitation frequencies, (a) $\Omega = 0.7 \ \ \omega_p$ - far from the resonant state and (b) $\Omega = 1.1 \ \ \omega_p$ - close to the resonant state (beating phenomenon).

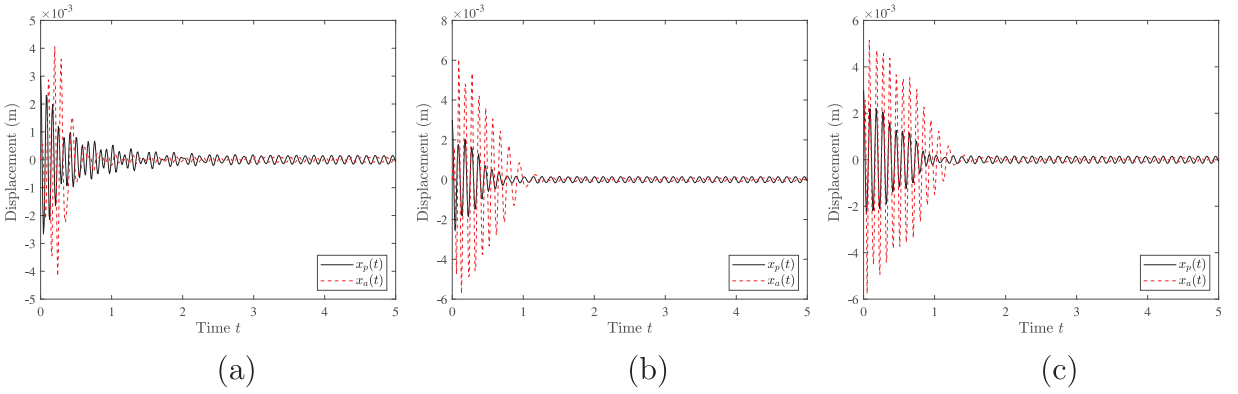

Fig. 13. The time responses of the displacements $x_p(t)$ and $x_a(t)$ for different values of the nonlinear stiffness parameter K, (a) 0.1 K, (b) 0.4 K, (c) 0.8 K, where $\Omega = 0.7 \ \ \omega_p$ and $R_{load} = 25 \ \ \Omega$.

Here, direct numerical integration is used (ode45 in Matlab) for solving the system given in Eq. (1) and Eq. (2) for different values of the nonlinear stiffness parameter K, resistance load R_{load} and small values of the amplitude of the external base excitation $Y = 0.8 \times 10^{-4}$. From the physical viewpoint, these two parameters are directly related to the overall stiffness and damping of the presented system. If these are optimally combined, it is possible to achieve both initial aims, i.e. vibration suppression and energy harvesting. For better understanding of the energy transfer and localisation phenomenon, the following initial conditions are adopted $x_p(0) = 3 \times 10^{-3} m, \ \ \dot{x}_p(0) = 0$ in each presented time simulation. The zero initial conditions for the nonlinear attachment are assumed. It should be pointed out that two groups of simulations are presented i.e. the case when the excitation frequency is considered to be far from, and the case when it is close to the resonance state. Fig. 12 shows the time responses of the primary structure without the nonlinear attachment, for two values of the excitation frequencies ($\Omega/\omega_p = .7$ and $\Omega/\omega_p = 1.1$). When the values of the excitation frequency are close to one of the natural frequencies of the system, the beating phenomenon emerges. This case is observed in Fig. 12b), where one can notice the response in the form of a wave with modulated amplitude.

Fig. 13, illustrates time responses of the primary structure $x_p(t)$ and the nonlinear attachment $x_p(t)$ for the time period $T = 5 \ \ s$ and for different values of the nonlinear stiffness parameter K. It is evident that introducing the nonlinear attachment as an additional NES mass reduces the response amplitudes, showing very good performance in vibration suppression application. Due to the energy transfer phenomenon, energy moves from the primary excited structure to the nonlinear attachment i.e. NES mass, and then dissipates through the mechanical and electrical damping. This phenomenon is manifested in Fig. 13 in the form of a reduced amplitudes of the primary structure. Comparison of the response amplitudes $x_p(t)$ from Figs. 12 a) and 13 shows that the amplitude $x_p(t)$ of the NES-EH device decreases much faster then those of

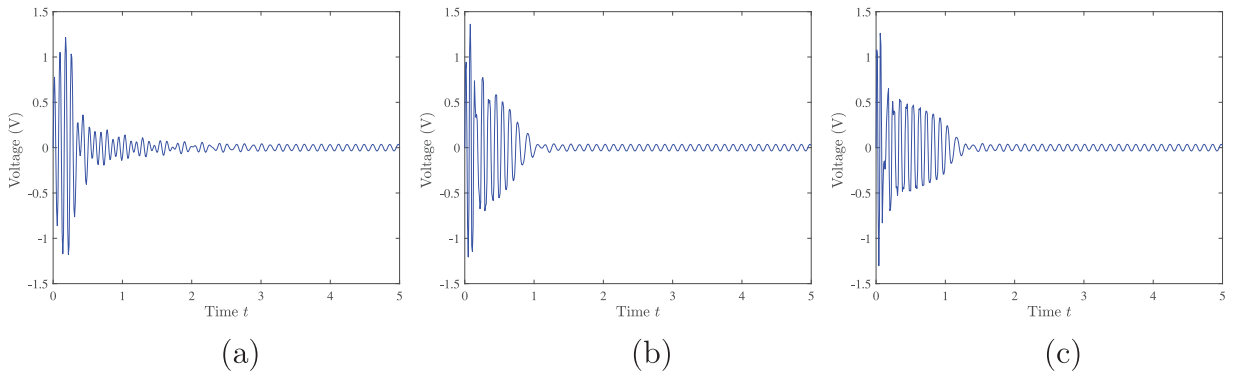

Fig. 14. The time responses of voltage across the load resistor for different values of the nonlinear stiffness parameter K, (a) 0.1 K, (b) 0.4 K, (c) 0.8 K, where $\Omega = 0.7\ \omega_p$ and $R_{load} = 25\ \Omega$.

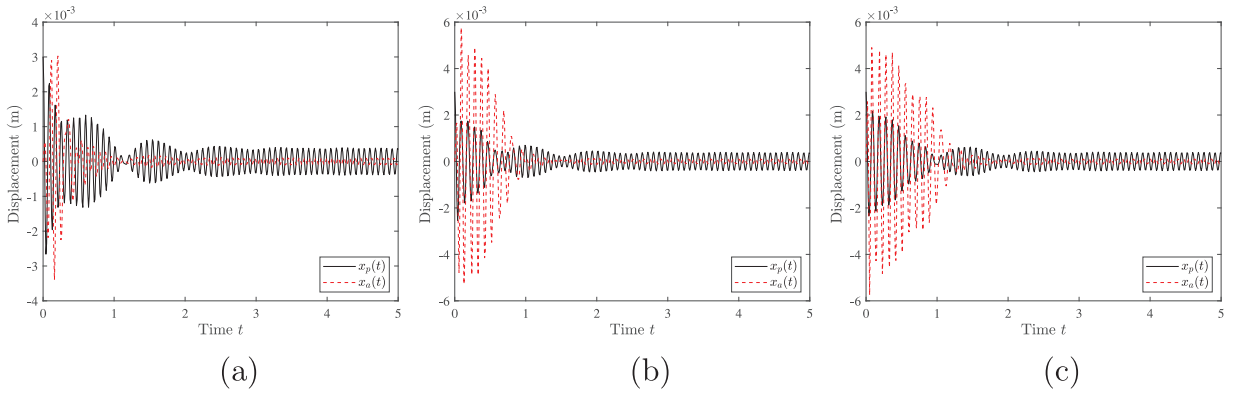

Fig. 15. The time responses of the displacements $x_p(t)$ and $x_a(t)$ for different values of the nonlinear stiffness parameter K, (a) 0.1 K, (b) 0.4 K, (c) 0.8 K, where $\Omega = 1.1\ \omega_p$ and $R_{load} = 25\ \Omega$.

the model with only the primary structure. By investigating the influence of the nonlinear stiffness parameter K on the vibration attenuation, it can be concluded that an increase in the parameter K leads to an increase in the amplitude $x_a(t)$ at the beginning of the simulation. Moreover, it can be observed that an increase of the nonlinear stiffness extends a time period that is necessary for attenuation of the response amplitudes $x_p(t)$ and $x_a(t)$. At the same time, the energy harvesting application can be analysed through the series of voltage response diagrams given in Fig. 14. It can be seen that at lower values of K, the response voltage $v(t)$ has higher values at the beginning of the simulation (maximum response voltage is close to $1V$) and then rapidly decreases. On the other hand, for higher values of the non-linear stiffness parameter K, one can observe a higher peak of the voltage response after which the amplitude of the voltage response gradually decreases to some finite small value. As already mentioned, setting the excitation frequency close to the resonant one (in this case $\Omega = 1.1\ \omega_p$) causes the beating phenomenon implying the reversible energy transfer between the primary structure and NES mass, Fig. 15. It can be noticed that the proposed NES-EH device shows advanced energy absorption characteristics, which is based on the fact that the energy is localized to the NES mass in some short time interval and then dissipated through damping [3]. Comparing the response diagrams obtained for different values of the nonlinear stiffness parameter K, it is found that an increase of the values of K decreases the influence of the beating phenomenon. On the other hand, Fig. 16 shows quite interesting application of beating phenomenon in amplification of the voltage response, which is most observable for higher values of the nonlinear stiffness parameter K (Fig. 16c)).

To further understand the effects of varying resistance load R_{load} on damping, time responses of the primary structure $x_p(t)$ and the nonlinear attachment $x_a(t)$ are presented in Figs. 17–20. From the electrical damping relation Eq. (3), it is obvious that an increase of the resistance load decreases a value of the electrical damping and therefore overall damping of the system, leading to larger oscillation amplitudes. Consequently, energy localisation to NES takes longer. Moreover, significantly higher response voltages are obtained for an increased load resistance R_{load} parameter, thus exhibiting improved harvesting properties. For higher excitation frequencies $\Omega = 1.1\ \omega_p$, which cause the beating phenomenon, the effects of the resistance load R_{load} become more prominent. It can be noticed that an increase of the parameter R_{load} leads to larger oscillations of the amplitude as shown in Fig. 19. This can blunt the effect of energy localization to NES and even make it impossible to complete the dissipation process of the transferred energy. Due to this fact, one should be careful during the design process of the combined NES-EH in order to avoid weak performance of the device. Further, Fig. 20 shows the voltage

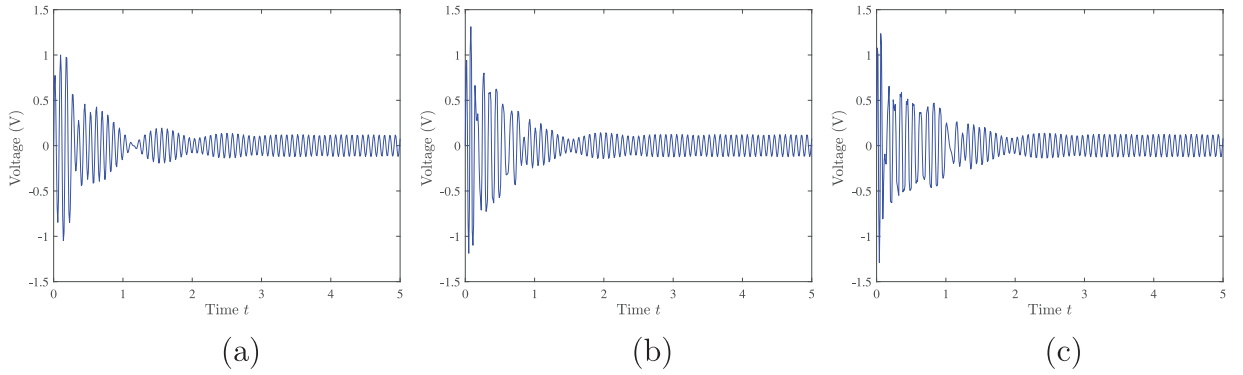

Fig. 16. The time responses of voltage across the load resistor for different values of the nonlinear stiffness parameter K, (a) 0.1 K, (b) 0.4 K, (c) 0.8 K, where $\Omega = 1.1 \ \omega_p$ and $R_{load} = 25 \ \Omega$.

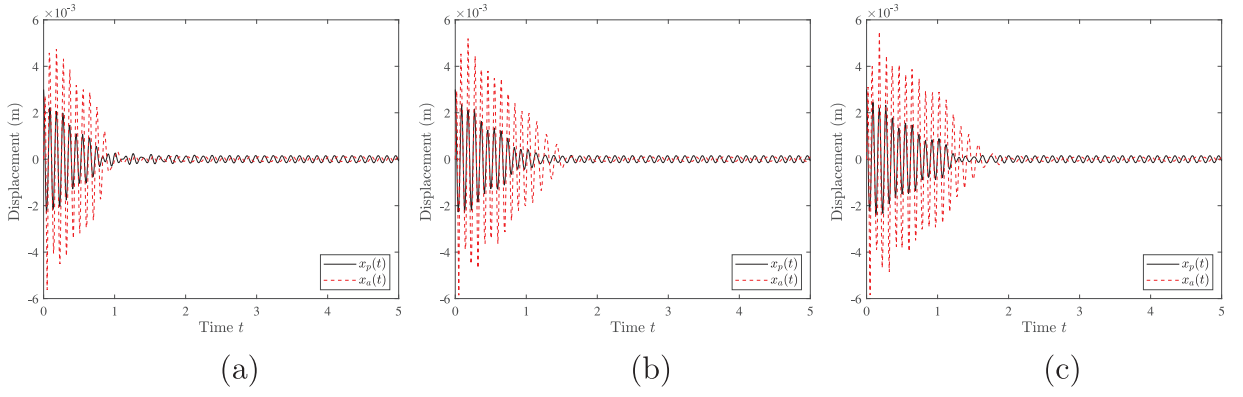

Fig. 17. The time responses of the displacements $x_p(t)$ and $x_a(t)$ for different values of the nonlinear stiffness parameter R_{load}, (a) $R_{load} = 12 \ \Omega$, (b) $R_{load} = 25 \ \Omega$, (c) $R_{load} = 50 \ \Omega$, where $\Omega = 0.7 \ \omega_p$.

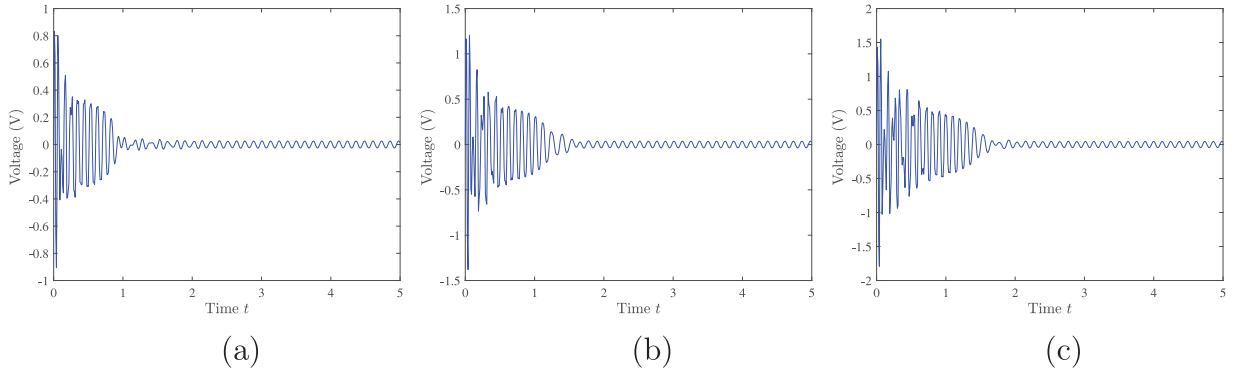

Fig. 18. The time responses of voltage across the load resistor for different values of the nonlinear stiffness parameter R_{load}, (a) $R_{load} = 12 \ \Omega$, (b) $R_{load} = 25 \ \Omega$, (c) $R_{load} = 50 \ \Omega$, where $\Omega = 0.7 \ \omega_p$.

responses for different values of the resistance load R_{load} excited in the beating regime. It can be observed that increasing the resistance load R_{load} reduces the electrical damping effect and, correspondingly, the overall system's damping, which yields higher voltage $v(t)$. Moreover, from Fig. 20 c) it is apparent that the beating phenomenon becomes more prominent, which results in higher estimated power of the energy harvester.

Finally, numerical results show that varying the nonlinear stiffness significantly mitigates the influence of the beating phenomenon on the response amplitude. Moreover, an increase of the nonlinear stiffness also reduces the estimated voltage response. From the physical point of view, the resistance load has a significant effect on overall damping in the system and the corresponding responses. Furthermore, when the system is excited with a frequency close to the resonant state, the

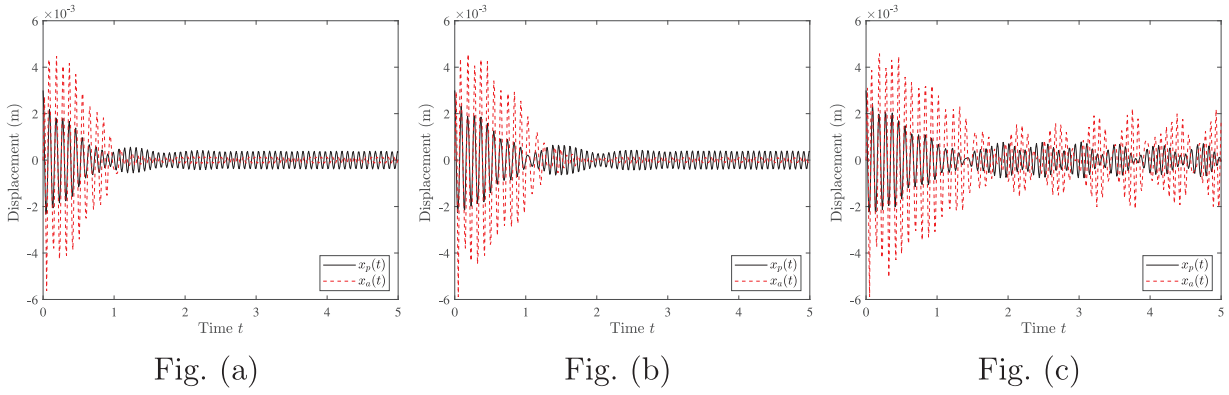

Fig. 19. The time responses of the displacements $x_p(t)$ and $x_a(t)$ for different values of the nonlinear stiffness parameter R_{load}, (a) $R_{load} = 12\ \ \Omega$, (b) $R_{load} = 25\ \ \Omega$, (c) $R_{load} = 50\ \ \Omega$, where $\Omega = 1.1\ \ \omega_p$.

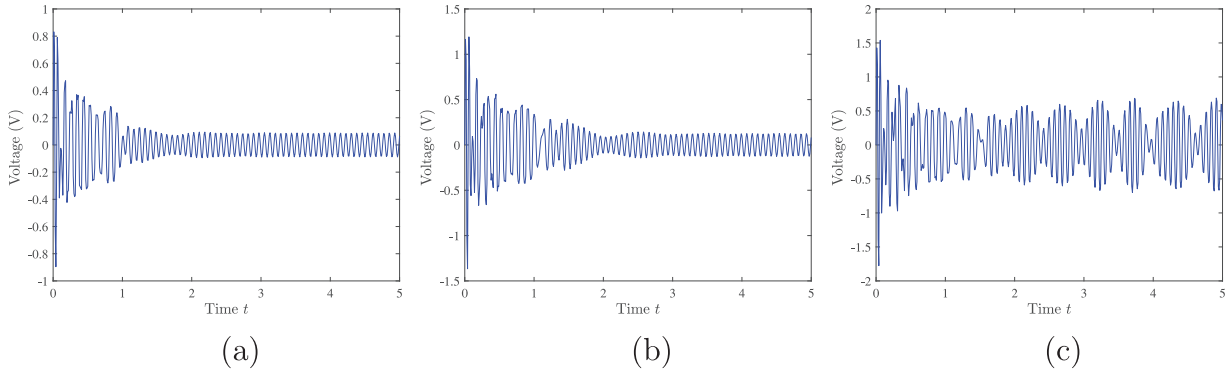

Fig. 20. The time responses of voltage across the load resistor for different values of the nonlinear stiffness parameter R_{load}, (a) $R_{load} = 12\ \ \Omega$, (b) $R_{load} = 25\ \ \Omega$, (c) $R_{load} = 50\ \ \Omega$, where $\Omega = 1.1\ \ \omega_p$.

influence of the resistance load on the response becomes more prominent. Satisfying NES performance is observed in all presented cases, where energy is localized in short time intervals.

7. Summary and conclusion

In this communication, the nonlinear dynamic behaviour of a two-degree of freedom NES-EH system subject to the periodic base excitation is investigated. The corresponding mathematical model of the system is presented in the form of two Duffing type nonlinear differential equations, where nonlinearity is introduced through a nonlinear spring. The electromagnetic phenomenon is employed for the energy harvester mechanism based on a magnet oscillating between two coils placed on the primary structure. Periodic responses in terms of the Fourier series are obtained by using the incremental harmonic balance (IHB) method in combination with the arc-length continuation technique, while the stability is investigated by using the Floquet theory. Completed set of integrals for the IHB method is derived in analytical form in order to reduce the computation time. The presented results show the effects of the attached NES mass to the primary structure response amplitude mitigation. In order to analyse the influence of different material parameters such as the nonlinear stiffness, resistance load, frequency and the amplitude of excitation force, the corresponding frequency and force response curves are traced and the time history diagrams are obtained.

The main focus in the parametric study is devoted to the analysis of the effects of resistance load and nonlinear stiffness parameter on the traced response amplitude - base amplitude, frequency-amplitude and time response curves. In conclusion, this study demonstrates significant influence of both parameters in reducing the response amplitudes of the system, especially at higher values of the excitation frequency. The unstable branch of the periodic response is detected between two saddle-node bifurcation points. The time response curves show the influence of NES in vibration attenuation and energy harvesting performance. The targeted energy transfer case is observed, where energy from the primary structure goes to the NES subsystem in very short time, i.e. the effect of energy localization occurs. The estimated output voltage during the vibration of NES-EH system appears to be significant and it is demonstrated that the system analysed herein can perform simultaneously as an energy source and vibration attenuation device.

Credit author statement

DK and MC developed the computational program and generated the results. SP wrote the discussions on the results. SA secured the funding, supervised the work and contributed towards the writing of the paper. All authors developed the scientific idea underpinning the paper together.

Declaration of Competing Interest

The authors declare that they have no conflict of interest.

Acknowledgements

Dr. D. Karličić and Prof. S. Adhikari were supported by the Marie Skdowska-Curie actions | Horizon 2020 - European Commission: 799201-METACTIVE. Dr. M.Cajić and S. Paunović were funded by the Serbian Ministry of Education, Science and Technological Development through the Mathematical Institute Serbian Academy of Science and Art.

References

[1] Frahm H.. Device for damping vibrations of bodies. US Patent1911; 989:958. April 18.
[2] Vakakis AF. Inducing passive nonlinear energy sinks in vibrating systems. J Vib Acoust 2001;123(3):324–32.
[3] Vakakis AF, Gendelman OV, Bergman LA, McFarland DM, Kerschen G, Lee YS. Nonlinear targeted energy transfer in mechanical and structural systems, volume 156. Springer Science & Business Media; 2008.
[4] Vakakis AF. Passive nonlinear targeted energy transfer. Philos Trans R Soc A 2018;376(2127):20170132.
[5] Lu Z, Wang Z, Zhou Y, Lu X. Nonlinear dissipative devices in structural vibration control: a review. J Sound Vib 2018;423:18–49.
[6] Gendelman OV. Transition of energy to a nonlinear localized mode in a highly asymmetric system of two oscillators. Nonlinear Dyn 2001;25(1):237–53.
[7] Gendelman OV. Bifurcations of nonlinear normal modes of linear oscillator with strongly nonlinear damped attachment. Nonlinear Dyn 2004;37(2):115–28.
[8] Starosvetsky Y, V Gendelman O. Response regimes of linear oscillator coupled to nonlinear energy sink with harmonic forcing and frequency detuning. J Sound Vib 2008;315(3):746–65.
[9] Malatkar P, Nayfeh AH. Steady-state dynamics of a linear structure weakly coupled to an essentially nonlinear oscillator. Nonlinear Dyn 2007;47(1–3):167–79.
[10] Enhancing the robustness of aeroelastic instability suppression using multi-degree-of-freedom nonlinear energy sinks. AIAA J 2008;46(6):1371–94.
[11] Bichiou Y, Hajj MR, Nayfeh AH. Effectiveness of a nonlinear energy sink in the control of an aeroelastic system. Nonlinear Dyn 2016;86(4):2161–77.
[12] Yan Z, Ragab SA, Hajj MR. Passive control of transonic flutter with a nonlinear energy sink. Nonlinear Dyn 2018;91(1):577–90.
[13] Mehmood A, Nayfeh AH, Hajj MR. Effects of a non-linear energy sink (nes) on vortex-induced vibrations of a circular cylinder. Nonlinear Dyn 2014;77(3):667–80.
[14] Blanchard A, Bergman LA, Vakakis AF. Vortex-induced vibration of a linearly sprung cylinder with an internal rotational nonlinear energy sink in turbulent flow. Nonlinear Dyn 2019:1–17.
[15] Erturk A, Inman DJ. Piezoelectric energy harvesting. John Wiley & Sons; 2011.
[16] Litak G, Friswell MI, Adhikari S. Magnetopiezoelastic energy harvesting driven by random excitations. Appl Phys Lett 2010;96(21):214103.
[17] Adhikari S, Friswell MI, Inman DJ. Piezoelectric energy harvesting from broadband random vibrations. Smart Mater Struct 2009;18(11):115005.
[18] Friswell MI, Ali SF, Bilgen O, Adhikari S, Lees AW, Litak G. Non-linear piezoelectric vibration energy harvesting from a vertical cantilever beam with tip mass. J Intell Mater Syst Struct 2012;23(13):1505–21.
[19] Ahmadabadi ZN, Khadem SE. Nonlinear vibration control and energy harvesting of a beam using a nonlinear energy sink and a piezoelectric device. J Sound Vib 2014;333(19):4444–57.
[20] Fang Z-W, Zhang Y-W, Xiang Li HD, Chen L-Q. Integration of a nonlinear energy sink and a giant magnetostrictive energy harvester. J Sound Vib 2017;391:35–49.
[21] Zhang Y, Tang L, Liu K. Piezoelectric energy harvesting with a nonlinear energy sink. J Intell Mater Syst Struct 2017;28(3):307–22.
[22] Xiong L, Tang L, Liu K, Mace BR. Broadband piezoelectric vibration energy harvesting using a nonlinear energy sink. J Phys D 2018;51(18):185502.
[23] Kremer D, Liu K. A nonlinear energy sink with an energy harvester: harmonically forced responses. J Sound Vib 2017;410:287–302.
[24] Kremer D, Liu K. A nonlinear energy sink with an energy harvester: transient responses. J Sound Vib 2014;333(20):4859–80.
[25] Fang Z-W, Zhang Y-W, Li X, Ding H, Chen L-Q. Complexification-averaging analysis on a giant magnetostrictive harvester integrated with a nonlinear energy sink. J Vib Acoust 2018;140(2):21009.
[26] Pogromsky A, van den Berg R. Frequency domain performance analysis of Lur'e systems. IEEE Trans Control Syst Technol 2014;22(5):1949–55.
[27] Pogromsky AY, Matveev AS. Stability analysis via averaging functions. IEEE Trans Automat Contr 2015;61(4):1081–6.
[28] Leung A, K Chui S. Non-linear vibration of coupled duffing oscillators by an improved incremental harmonic balance method. J Sound Vib 1995;181(4):619–33.
[29] Bhattiprolu U, Bajaj AK, Davies P. Periodic response predictions of beams on nonlinear and viscoelastic unilateral foundations using incremental harmonic balance method. Int J Solids Struct 2016;99:28–39.
[30] L Huang J, Su RKL, Y Lee Y, H Chen S. Nonlinear vibration of a curved beam under uniform base harmonic excitation with quadratic and cubic nonlinearities. J Sound Vib 2011;330(21):5151–64.
[31] Zhou S, Song G, Ren Z, Wen B. Nonlinear analysis of a parametrically excited beam with intermediate support by using multi-dimensional incremental harmonic balance method. Chaos Soliton Fract 2016;93:207–22.
[32] Du Y-z, Wang W-h, Wang L-l, Huang Y. Nonlinear dynamics of heave motion of the sandglass-type floating body with piecewise-nonlinear, time-varying stiffness. Mar Struct 2018;60:136–50.
[33] Wang S, Hua L, Yang C, Han X, Su Z. Applications of incremental harmonic balance method combined with equivalent piecewise linearization on vibrations of nonlinear stiffness systems. J Sound Vib 2019;441:111–25.
[34] Kong X, Li H, Wu C. Dynamics of 1-dof and 2-dof energy sink with geometrically nonlinear damping: application to vibration suppression. Nonlinear Dyn 2018;91(1):733–54.
[35] Wang S, Hua L, Yang C, Tan X, et al. Nonlinear vibrations of a piecewise-linear quarter-car truck model by incremental harmonic balance method. Nonlinear Dyn 2018;92(4):1719–32.
[36] Nayfeh AH, Balachandran B. Applied nonlinear dynamics: analytical, computational, and experimental methods. John Wiley & Sons; 2008.
[37] Seydel R. Practical bifurcation and stability analysis, volume 5. Springer Science & Business Media; 2009.
[38] L Huang J, Su RKL, H Chen S. Precise Hsu's method for analyzing the stability of periodic solutions of multi-degrees-of-freedom systems with cubic nonlinearity. Comput Struct 2009;87(23–24):1624–30.

[39] Shen JH, Lin KC, Chen SH, Sze KY. Bifurcation and route-to-chaos analyses for Mathieu–Duffing oscillator by the incremental harmonic balance method. Nonlinear Dyn 2008;52(4):403–14.
[40] Shen Y, Yang S, Liu X. Nonlinear dynamics of a spur gear pair with time-varying stiffness and backlash based on incremental harmonic balance method. Int J Mech Sci 2006;48(11):1256–63.
[41] Huang JL, Zhu WD. Nonlinear dynamics of a high-dimensional model of a rotating euler–bernoulli beam under the gravity load. J Appl Mech 2014;81(10).
[42] Jiang X, McFarland DM, Bergman LA, Vakakis AF. Steady state passive nonlinear energy pumping in coupled oscillators: theoretical and experimental results. Nonlinear Dyn 2003;33(1):87–102.
[43] Dhooge A, Govaerts W, Kuznetsov YA. Matcont: a Matlab package for numerical bifurcation analysis of odes. ACM Trans Math Softw 2003;29(2):141–64.